20^{th} International Conference on Composite Materials
Copenhagen, 19-24^{th} July 2015

FULL-FIELD STRESS TAILORING OF COMPOSITE LAMINATES

Rainer M.J. Groh[1] and Paul M. Weaver[2]

[1]Advanced Composites Centre for Innovation and Science,
University of Bristol, Queen's Building, University Walk, Bristol, BS8 1TR, UK
Email: rainer.groh@bristol.ac.uk, web page: www.bristol.ac.uk/composites

[2] Email: paul.weaver@bristol.ac.uk

Keywords: Higher-order modelling, Variable Stiffness, Structural Tailoring

Abstract

The Hellinger-Reissner mixed variational principle is used to derive a higher-order zig-zag theory for the stretching and bending of highly heterogeneous, laminated, variable stiffness beams. The derivation is presented in generalised form such that the order of the theory can be chosen a priori without the need for re-writing the governing equations. The model is used to analyse the bending of variable stiffness beams under different boundary conditions and validated against 3D finite element results. Combined with findings in previous work the present model captures the full 3D stress field of laminated beams accurately without the need for a posteriori stress recovery steps. The model is then used within a genetic algorithm to find a compromise between maximising bending stiffness and minimising the likelihood of delaminations in simply-supported and clamped beams. It is found that the greater design space of variable stiffness laminates facilitates a better compromise compared to quasi-isotropic straight-fiber laminates. This enhanced response is possible because variable stiffness laminates can be designed to guarantee high global bending stiffness while locally tailoring the 3D stress-field at areas of stress-concentration to delay the onset of delaminations. Thus, the present work shows the capability of variable stiffness laminates to favourably re-distribute through-thickness stresses.

1 INTRODUCTION

The application of multi-layered composite materials in load-bearing structures is finding widespread application particularly in the aeronautical, marine and renewable energy industries. Reasons include their high specific strength and stiffness, good fatigue resistance and enhanced design freedom on a micro- and macromechanical level.

In these industries the design of primary load-bearing structures requires accurate tools for stress analysis. When used around areas of stress concentration or in fail-safe design frameworks composite laminates are often designed to have thicker cross-sections. Under these circumstances non-classical effects, such as transverse shear and normal deformation become important factors in the failure event. These considerations mean that Euler-Bernoulli beam and Kirchhoff plate/shell models that underpin Classical Laminate Analysis (CLA) [1] inaccurately predict global and local deformations. Transverse shear deformations are particularly pronounced in composite materials because the ratio of longitudinal to shear modulus is approximately one order of magnitude larger than for isotropic materials ($E_{iso}/G_{iso} = 2.6$, $E_{11}/G_{xz} \approx 140/5 = 28$). The analysis of layered composites is also more cumbersome due to transverse anisotropy, and interlaminar continuity conditions on displacement, transverse shear and transverse normal stress fields.

Most notably, transverse anisotropy, i.e. the difference in layerwise transverse shear and normal moduli, leads to sudden changes in slope of the three displacement fields u_x, u_y, u_z at layer interfaces. This is known as the zig-zag phenomenon. While interlaminar continuity of the displacements requires u_x, u_y, u_z to be C^0 continuous at interfaces, interfacial continuity of the transverse stresses forces the displacement fields to be C^1 *discontinuous*. Therefore, accurate models for stress analysis

of multi-layered composite and sandwich structures should ideally address the higher-order effects such as transverse shear and tranverse normal deformation, and zig-zag displacement fields.

For this purpose high-fidelity 3D Finite Element (FE) models are often used. However, these models can become computationally prohibitive when employed for laminates with large number of layers, in optimisation studies, for non-linear problems that require iterative solution techniques or for progressive failure analyses. Thus, with the aim of developing rapid, yet robust design tools for practical purposes there remains a need for further efficient modelling techniques. In this regard particular focus is required on equivalent single layer (ESL) theories because the number of unknowns in these formulations is independent of the number of layers.

In the field of axiomatic structural models purely displacement-based formulations have received the most interest. One of the earliest examples that adressed non-classical effects was the First Order Shear Deformation Theory (FSDT) [2–4]. However, as Whitney & Pagano [5] demonstrate, FSDT only yields improvements over CLA for global structural phenomenon but does not improve in-plane strain and stress predictions for highly heterogeneous and thick laminates. Furthermore, FSDT produces piecewise constant transverse shear stresses that violate interfacial continuity and equilibrium of tractions at the top and bottom surfaces. To overcome these shortcomings the so-called Higher-Order Shear Deformation Theories (HOT) were introduced. In general, the cross-section is allowed to deform in any form by including higher-order terms in the axiomatic expansions of the in-plane displacements u_x and u_y. The resulting transverse shear stresses derived from kinematic and constitutive equations are not enforced to satisfy equilibrium at the interfaces of individual layers, or at the top and bottom surfaces. However, it can be shown that as the order of the theory is increased, the transverse shear stresses converge to satisfy these equilibrium conditions [6]. In this regard, the unified formulations by Carrera [7] and Demasi [8] are useful modelling frameworks, as the order of the theory can be increased a priori without re-deriving the governing equations. The order of the theory required to capture the higher-order shear effects depends on the orthotropy ratio $\frac{E}{G}\left(\frac{t}{L}\right)^2$ where E and G are pertinent axial and transverse shear modulii, respectively, and t and L are thickness and the smallest in-plane dimension, respectively. Thus, as the magnitude of the orthotropy ratio increases the number of variables required to accurately model the higher-order behaviour increases accordingly.

To reduce the number of variables Vlasov [9] refined Mindlin's theory by enforcing the equilibrium of surface tractions explicitly. Taking Vlasov's condition into consideration, Reddy [10] presented a higher-order shear deformation theory by expanding the in-plane displacement field to a third order polynomial in z. A large number of different shear shape functions have been published in the past ranging from polynomial [11–13] to trigonometric [14–18], hyperbolic [19, 20] and exponential [21, 22]. By enforcing that the assumed displacement field leads to equilibrium of transverse shear tractions at the surfaces many of these theories condense the number of variables in the in-plane displacement assumptions for u_x and u_y by introducing the Euler-Kirchhoff rotations $\frac{\partial w}{\partial x}$ and $\frac{\partial w}{\partial y}$. However, this leads to a static inconsistency between the shear forces derived from equilibrium and constitutive equations and artificially stiffens the structure at clamped edges [6]. Furthermore, in the case of layered structures the transverse shear stress profiles do not obey the interfacial continuity conditions on transverse shear stresses. As a result, most displacement-based theories rely on post-processing steps to recover accurate transverse stresses from Cauchy's 3D indefinite equilibrium equations.

This post-processing operation can be precluded if some form of stress assumption is made. One class of model is based on applying the Hellinger-Reissner mixed variational principle. Here the strain energy is written in complementary form in terms of in-plane and transverse stresses, and the transverse equilibrium equation is introduced as a constraint condition using a Lagrange multiplier [23, 24]. Batra & Vidoli [25] and Batra et al. [26] used the Hellinger-Reissner mixed variational theorem to develop a higher-order theory for studying vibrations and plane waves in piezoelectric and anisotropic plates, accounting for both transverse shear and transverse normal deformations with all functional unknowns expanded in the thickness direction using orthonormal Legendre polynomials. The researchers showed that the major advantage of the Hellinger-Reissner theory is that by enforcing stresses to satisfy the natural boundary conditions at the top and bottom surfaces, and deriving transverse stresses from the plate equations directly, the stress fields are closer to 3D elasticity

solutions than a pure displacement-based equivalent that relies on Hooke's law to derive the stress fields. In particular this means that boundary layers near clamped and free edges, and asymmetric stress profiles due to surface tractions on one surface only can be captured accurately. Cosentino & Weaver [27] applied the Hellinger-Reissner principle to symmetrically laminated straight-fibre composites to develop a single sixth-order differential equation in just two variables: transverse deflection w and stress function Ω. The formulation of this theory is less general than the one proposed by Batra & Vidoli [25] as its aims are to realise accurate 3D dimensional stress predictions for practical composite laminates at minimum computational cost.

Recently, Tessler et al. developed the so-called refined zig-zag theory (RZT) [28–31], which enhances the displacement assumption of FSDT with a zig-zag field $\psi_\alpha(x, y)$ multiplied by a piecewise continuous transverse function ϕ^k_α,

$$u^{(k)}_\alpha(x, y, z) = u_\alpha + z\theta_\alpha + \phi^{(k)}_\alpha(z)\psi_\alpha \quad \text{for} \quad \alpha = x, y \tag{1a}$$

$$u_z(x, y, z) = w(x, y). \tag{1b}$$

In this theory the zig-zag slopes $\beta_x = \partial\phi^{(k)}_x/\partial z$ and $\beta_y = \partial\phi^{(k)}_y/\partial z$ for u_x and u_y, respectively, are defined by the difference between the transverse shear rigidity of a layer $G_{\alpha z}$, and the effective transverse shear rigidity G of the entire layup

$$\beta^k_\alpha = \frac{G^k_{\alpha z}}{G_\alpha} - 1, \quad \text{and} \quad G_\alpha = \left[\frac{1}{t}\sum_{k=1}^{N}\frac{t^k}{G_{\alpha z}}\right]^{-1} \tag{2}$$

where t^k and t are the thickness of the layer k and total laminate thickness, respectively.

In recent work [32] the present authors showed that a zig-zag theory based on the Hellinger-Reissner mixed variational theory using the RZT zig-zag function accurately captures the full 3D stress field of beams to within 1% of Pagano's elasticity solution for highly heterogeneous anisotropic materials with thickness to length ratios of 1:8. Furthermore, localised boundary layers of the stress fields towards support conditions can be captured. In Section 2 of this paper the theory presented in [32] is extended to composite beams where the fibre orientations in each ply may vary along the length. The aim of the work is to use this model to to tailor the through-thickness transverse stress fields by taking advantage of the large design space of variable stiffness composites. As through-thickness damage, such as delaminations, are driven by tranvserse shear and transverse normal stresses the possibility exists to tailor the through-thickness stress fields to reduce the chance of delaminations. The accuracy of the theory is validated in Section 3.1 and an optimisation study is presented in Section 3.2 to maximise the flexural stiffness of a beam in bending while minimising the likelihood of developing delaminations.

2 THEORY

This section outlines the derivation of the transverse shear stress and transverse normal stress assumption from a higher-order axial stress field. These three stress assumptions are then used to derive a set of governing equations using the Hellinger-Reissner mixed variational principle.

2.1 Derivation of governing equations

2.1.1 Derivation of in-plane and transverse stress fields

We assume a generalised in-plane displacement field of the form,

$$u^{(k)}_x(x, z) = u_0 + z\theta + z^2\zeta + z^3\xi + \cdots + \phi^{(k)}(z)\psi \tag{3}$$

where u_0 is the reference surface axial displacement, θ is the rotation of the beam cross-section, $\zeta, \xi, \ldots$ are higher-order rotations, ψ is the zig-zag rotation and $\phi^{(k)}$ is a pertinent zig-zag function where superscript (k) refers to ply k. In condensed matrix form the Eq. (3) reads

$$u^{(k)}_x(x, z) = \boldsymbol{f}_g\mathcal{U}_g + \phi^{(k)}\psi \tag{4}$$

where $\mathcal{U}_g$ and ψ are the global and local displacement fields, respectively and the global row vector $\boldsymbol{f}_g$ describes the global through-thickness displacement variation,

$$\boldsymbol{f}_g(z) = \begin{bmatrix} 1 & z & z^2 & z^3 & \dots \end{bmatrix}, \qquad \mathcal{U}_g = \begin{bmatrix} u_0 & \theta & \zeta & \xi & \dots \end{bmatrix}^T. \tag{5}$$

Thus the in-plane strain is given by,

$$\epsilon_x^{(k)} = u_{x,x}^{(k)} = \boldsymbol{f}_g \mathcal{U}_{g,x} + \phi_{,x}^{(k)} \psi + \phi^{(k)} \psi_{,x} = \boldsymbol{f}_g \epsilon_g + \boldsymbol{f}_l \epsilon_l \tag{6}$$

where the comma notation is employed to denoted differentiation, and the local strain field ϵ_g and local row vector $\boldsymbol{f}_l$ are given by,

$$\boldsymbol{f}_l(z) = \begin{bmatrix} \phi_{,x}^{(k)} & \phi^{(k)} \end{bmatrix}, \qquad \epsilon_l = \begin{bmatrix} \psi & \psi_{,x} \end{bmatrix}^T. \tag{7}$$

Thus, the axial strain field in Eq. (6) is written as a combination of a global higher-order (independent of local ply properties) and a local zig-zag strain field (dependent on local ply properties). In general, most zig-zag functions in the literature can be written in the linear form

$$\phi^{(k)}(z) = g_{ZZF}^{(k)} \cdot z + c_{ZZF}^{(k)}. \tag{8}$$

The zig-zag function terms $g_{ZZF}^{(k)}$ and $c_{ZZF}^{(k)}$ used in RZT are derived from material properties and may vary with location x. Murakami's zig-zag function [33] assumes alternating values of $+1$ and -1 at top and bottom interfaces regardless of location. In this case the derivative $\phi_{,x}^{(k)}$ and associated displacement unknown ψ vanish in Eq. (6) and (7).

Using the constitutive equation the axial stress field is derived from the axial strain in Eq. (6)

$$\sigma_x^{(k)} = \bar{Q}^{(k)} \epsilon_x^{(k)} = \bar{Q}^{(k)} \left(\boldsymbol{f}_g \epsilon_g + \boldsymbol{f}_l \epsilon_l \right). \tag{9}$$

The in-plane stress resultants are derived as follows,

$$\mathcal{F}_g = \int_{-t/2}^{t/2} \boldsymbol{f}_g^T \sigma_x^{(k)} \mathrm{d}z = \int_{-t/2}^{t/2} \left(\boldsymbol{f}_g^T \bar{Q}^{(k)} \boldsymbol{f}_g \epsilon_g + \boldsymbol{f}_g^T \bar{Q}^{(k)} \boldsymbol{f}_l \epsilon_l \right) \mathrm{d}z = \boldsymbol{S}_{gg} \epsilon_g + \boldsymbol{S}_{gl} \epsilon_l \tag{10}$$

$$\mathcal{F}_l = \int_{-t/2}^{t/2} \boldsymbol{f}_l^T \sigma_x^{(k)} \mathrm{d}z = \int_{-t/2}^{t/2} \left(\boldsymbol{f}_l^T \bar{Q}^{(k)} \boldsymbol{f}_g \epsilon_g + \boldsymbol{f}_l^T \bar{Q}^{(k)} \boldsymbol{f}_l \epsilon_l \right) \mathrm{d}z = \boldsymbol{S}_{lg} \epsilon_g + \boldsymbol{S}_{ll} \epsilon_l \tag{11}$$

where the superscript T denotes the transpose of a matrix, and $\boldsymbol{S}_{gg}$, $\boldsymbol{S}_{gl}$, $\boldsymbol{S}_{gl}$ and $\boldsymbol{S}_{ll}$ are the global, local and global-local coupling stiffness matrixes,

$$\boldsymbol{S}_{gg} = \int_{-t/2}^{t/2} \boldsymbol{f}_g^T \bar{Q}^{(k)} \boldsymbol{f}_g \mathrm{d}z, \quad \boldsymbol{S}_{gl} = \int_{-t/2}^{t/2} \boldsymbol{f}_g^T \bar{Q}^{(k)} \boldsymbol{f}_l \mathrm{d}z, \tag{12}$$

$$\boldsymbol{S}_{lg} = \int_{-t/2}^{t/2} \boldsymbol{f}_l^T \bar{Q}^{(k)} \boldsymbol{f}_g \mathrm{d}z, \quad \boldsymbol{S}_{ll} = \int_{-t/2}^{t/2} \boldsymbol{f}_l^T \bar{Q}^{(k)} \boldsymbol{f}_l \mathrm{d}z. \tag{13}$$

Thus the relation between stress resultants and strain variables is given by

$$\begin{pmatrix} \mathcal{F}_g \\ \mathcal{F}_l \end{pmatrix} = \begin{bmatrix} \boldsymbol{S}_{gg} & \boldsymbol{S}_{gl} \\ \boldsymbol{S}_{lg} & \boldsymbol{S}_{ll} \end{bmatrix} \begin{pmatrix} \epsilon_g \\ \epsilon_l \end{pmatrix} \Rightarrow \mathcal{F} = \boldsymbol{S} \epsilon \quad \text{and} \quad \epsilon = \boldsymbol{s} \mathcal{F} \quad \text{where} \quad \boldsymbol{s} = \boldsymbol{S}^{-1} \tag{14}$$

where $\boldsymbol{S}$ is the stiffness matrix of membrane and flexural rigidities, and its inverse $\boldsymbol{s}$ is the compliance matrix. The equation for in-plane stress in Eq. (9) can now be recast in terms of stress resultants $\mathcal{F}$,

$$\sigma_x^{(k)} = \bar{Q}^{(k)} \begin{bmatrix} \boldsymbol{f}_g & \boldsymbol{f}_l \end{bmatrix} \begin{pmatrix} \epsilon_g \\ \epsilon_l \end{pmatrix} = \bar{Q}^{(k)} \boldsymbol{f}^{(k)} \epsilon = \bar{Q}^{(k)} \boldsymbol{f}^{(k)} \boldsymbol{s} \mathcal{F}. \tag{15}$$

The axial stress field of this higher-order theory, written in terms of the stress resultants $\mathcal{F}$ is used to derive expressions for the transverse shear and transverse normal stress fields.

An expression for the transverse shear stress is found by integrating the axial stress of Eq. (15) in Cauchy's indefinite equilibrium equation,

$$\tau_{xz}^{(k)} = -\int \frac{\mathrm{d}\sigma_x}{\mathrm{d}x} \, \mathrm{d}z = -\frac{\mathrm{d}}{\mathrm{d}x} \left(\bar{Q}^{(k)} \left(\int \boldsymbol{f}^{(k)} \, \mathrm{d}z \right) \boldsymbol{s} \mathcal{F} \right) = -\frac{\mathrm{d}}{\mathrm{d}x} \left[\bar{Q}^{(k)} \boldsymbol{g}^{(k)} \boldsymbol{s} \mathcal{F} \right] + \boldsymbol{a}^{(k)} \tag{16}$$

where $\boldsymbol{g}^{(k)}(z)$ captures the variation of $\tau_{xz}^{(k)}$ through each ply k of the laminate.

The N layerwise constants $\boldsymbol{a}^{(k)}$ are found by enforcing $N-1$ interfacial continuity conditions $\tau_{xz}^{(k)}(z_{k-1}) = \tau_{xz}^{(k-1)}(z_{k-1})$ and one of the prescribed surface tractions, i.e. either the bottom surface $\tau_{xz}^{(1)}(z_0) = \hat{T}_b$ or the top surface $\tau_{xz}^{(N)}(z_N) = \hat{T}_t$. Here we choose to enforce the bottom surface traction such that the layerwise integration constants $\boldsymbol{a}^k$ are found to be

$$\boldsymbol{a}^{(k)} = \sum_{i=1}^{k} \frac{\mathrm{d}}{\mathrm{d}x}\left[\left\{\bar{Q}^{(i)}\boldsymbol{g}^{(i)}(z_{i-1}) - \bar{Q}^{(i-1)}\boldsymbol{g}^{(i-1)}(z_{i-1})\right\}\boldsymbol{s}\mathcal{F}\right] + \hat{T}_b = \frac{\mathrm{d}}{\mathrm{d}x}\left[\boldsymbol{\alpha}^{(k)}\boldsymbol{s}\mathcal{F}\right] + \hat{T}_b \quad (17)$$

where by definition $\bar{Q}^0 = 0$. In the derivation of Eq. (17) the surface traction on the top surface is not enforced explicitly. However, this condition is automatically satisfied if equilibrium of the axial stress field Eq. (15) and transverse shear stress Eq. (16) is guaranteed. This derivation is the same as presented in [32] for constant stiffness laminates and therefore ommitted here for conciseness.

Next, an expression for the transverse normal stress is derived in a similar fashion. Integrating Cauchy's transverse equilibrium equation yields

$$\begin{aligned}\sigma_z^{(k)} &= -\int \frac{\mathrm{d}\tau_{xz}}{\mathrm{d}x}\mathrm{d}z = \frac{\mathrm{d}^2}{\mathrm{d}x^2}\left[\bar{Q}^{(k)}\int\left(\boldsymbol{g}^{(k)} - \boldsymbol{\alpha}^{(k)}\right)\mathrm{d}z\boldsymbol{s}\mathcal{F}\right] - \hat{T}_{b,x}z \\ &= \frac{\mathrm{d}^2}{\mathrm{d}x^2}\left[\left\{\bar{Q}^{(k)}\boldsymbol{h}^{(k)} - \boldsymbol{\alpha}^{(k)}z\right\}\boldsymbol{s}\mathcal{F}\right] - \hat{T}_{b,x}z + \boldsymbol{b}^{(k)} \end{aligned} \quad (18)$$

where $\boldsymbol{h}^{(k)}(z)$ captures the variation of $\sigma_z^{(k)}$ through each ply k of the laminate.

The N layerwise constants $\boldsymbol{b}^{(k)}$ are found by enforcing the $N-1$ continuity conditions $\sigma_z^{(k)}(z_{k-1}) = \sigma_z^{(k-1)}(z_{k-1})$ and one of the prescribed surface tractions, i.e. either the bottom surface $\sigma_z^{(1)}(z_0) = \hat{P}_b$ or the top surface $\sigma_z^{(N)}(z_N) = \hat{P}_t$. Thus by enforcing the $N-1$ continuity conditions and $\sigma_z^{(1)}(z_0) = \hat{P}_b$,

$$\boldsymbol{b}^{(k)} = \sum_{i=1}^{k} \frac{\mathrm{d}^2}{\mathrm{d}x^2}\left[\left\{\bar{Q}^{(i-1)}\boldsymbol{h}^{(i-1)}(z_{i-1}) - \bar{Q}^{(i)}\boldsymbol{h}^{(i)}(z_{i-1}) + \left(\boldsymbol{\alpha}^{(i)} - \boldsymbol{\alpha}^{(i-1)}\right)z_{i-1}\right\}\boldsymbol{s}\mathcal{F}\right] + \hat{T}_{b,x}z_0 + \hat{P}_b$$

$$\boldsymbol{b}^{(k)} = \frac{\mathrm{d}^2}{\mathrm{d}x^2}\left[\boldsymbol{\beta}^{(k)}\boldsymbol{s}\mathcal{F}\right] + \hat{T}_{b,x}z_0 + \hat{P}_b \quad (19)$$

where by definition $\bar{Q}^0 = \boldsymbol{\alpha}^0 = 0$. In the derivation of Eq. (19) the surface normal traction on the top surface is not enforced explicitly. However, this condition is automatically satisfied if equilibrium of the transverse shear stress field Eq. (16) and transverse normal stress Eq. (18) is guaranteed. This derivation is the same as presented in [32] for constant stiffness laminates and therefore ommitted here for conciseness.

Finally, the layerwise coefficients in the equations for $\tau_{xz}^{(k)}$ and $\sigma_z^{(k)}$, Eqs. (16) and (18) respectively, are each combined conveniently into single layerwise vectors such that,

$$\tau_{xz}^{(k)} = \frac{\mathrm{d}}{\mathrm{d}x}\left[\boldsymbol{c}^{(k)}\boldsymbol{s}\mathcal{F}\right] + \hat{T}_b \quad (20a)$$

$$\sigma_z^{(k)} = \frac{\mathrm{d}^2}{\mathrm{d}x^2}\left[\boldsymbol{e}^{(k)}\boldsymbol{s}\mathcal{F}\right] - \hat{T}_{b,x}\left(z - z_0\right) + \hat{P}_b. \quad (20b)$$

2.1.2 Hellinger-Reissner mixed variational principle

A new set of equilibrium equations is derived by means of minimising the potential energy functional Π defined in Castigliano's Theorem of Least Work. In this case, Π is a functional of the stress resultants $\mathcal{F}$ that define the internal strain energy of the beam and the work done by external tractions. Both the in-plane and transverse Cauchy equilibrium equations need to be satisfied to guarantee that the transverse stresses are recovered accurately. The Cauchy equations of an equivalent single layer are derived by integrating the indefinite equilibrium equation through the thickness z-direction,

$$\int_{z_0}^{z_N}\sigma_{x,x}\mathrm{d}z + \int_{z_0}^{z_N}\tau_{xz,z}\mathrm{d}z = N_{,x} + \tau_{xz}^{(N)}(z_N) - \tau_{xz}^{(1)}(z_0) = N_{,x} + \hat{T}_t - \hat{T}_b = 0 \quad (21)$$

$$\int_{z_0}^{z_N}\tau_{xz,x}\mathrm{d}z + \int_{z_0}^{z_N}\sigma_{z,z}\mathrm{d}z = Q_{,x} + \sigma_z^{(N)}(z_N) - \sigma_z^{(1)}(z_0) = Q_{,x} + \hat{P}_t - \hat{P}_b = 0. \quad (22)$$

Next, transverse shear force Q is eliminated from Eq. (22) using the moment equilibrium condition,

$$\begin{aligned}&\int_{z_0}^{z_N} z\left(\sigma_{x,x}+\tau_{xz,z}\right)\mathrm{d}z = M_{,x} - Q + z_N\hat{T}_t - z_0\hat{T}_b = 0\\ &\therefore Q = M_{,x} + z_N\hat{T}_t - z_0\hat{T}_b\end{aligned} \tag{23}$$

such that equilibrium equation (22) becomes

$$M_{,xx} + z_N\hat{T}_{t,x} - z_0\hat{T}_{b,x} + \hat{P}_t - \hat{P}_b = 0. \tag{24}$$

For equilibrium of the system the first variation of the potential energy functional Π must vanish in such a manner that equilibrium equations (21) and (24) are satisfied over the whole beam domain $x \in [x_A, x_B]$. Following the rules of the calculus of variations this condition is enforced using Lagrange multipliers $\lambda_1(x)$ and $\lambda_2(x)$, respectively, and adding these to the variation of functional Π,

$$\begin{aligned}\delta\Pi =& \delta\left[\frac{1}{2}\int_V \left(\sigma_x\epsilon_x + \tau_{xz}\gamma_{xz} + \sigma_z\epsilon_z\right)\mathrm{d}V - \int_{S_2}\left(\sigma_x\hat{u}_x^{(k)} + \tau_{xz}\hat{w}\right)\mathrm{d}S_2 + \right.\\ &\left.\int \lambda_1\left(N_{,x} + \hat{T}_t - \hat{T}_b\right)\mathrm{d}x + \int\lambda_2\left(M_{,xx} + z_N\hat{T}_{t,x} - z_0\hat{T}_{b,x} + \hat{P}_t - \hat{P}_b\right)\mathrm{d}x\right] = 0\end{aligned} \tag{25}$$

where $\hat{u}_x^{(k)}$ and $\hat{w}$ are the displacements defined on the boundary curve S_2.

In Eq. (25) the quantities σ_x, τ_{xz} and σ_z are defined by Eqs. (15), (20a) and (20b), respectively. The transverse shear strain $\gamma_{xz}^{(k)}$ is defined using the constitutive equation

$$\gamma_{xz}^{(k)} = \frac{\tau_{xz}^{(k)}}{G_{xz}^{(k)}} = \frac{1}{G_{xz}^{(k)}}\left(\boldsymbol{c}^{(k)}\boldsymbol{s}\mathcal{F}_{,x} + \hat{T}_b\right). \tag{26}$$

The transverse normal strain $\epsilon_z^{(k)}$ is derived from Hooke's Law, written in terms of the full compliance matrix $\bar{S}_{ij}$ in a state of plane strain in y, as this is the condition assumed in Section 3. Thus,

$$\begin{aligned}\epsilon_z^{(k)} &= R_{13}^{(k)}\sigma_x^{(k)} + R_{33}^{(k)}\sigma_z^{(k)}, \text{ where } R_{ij} = S_{ij} - \frac{S_{i2}S_{j2}}{S_{22}}\\ &= R_{13}^{(k)}\bar{Q}^{(k)}\boldsymbol{f}^{(k)}\boldsymbol{s}\mathcal{F} + R_{33}^{(k)}\left[\frac{\mathrm{d}^2}{\mathrm{d}x^2}\left(\boldsymbol{e}^{(k)}\boldsymbol{s}\mathcal{F}\right) - \hat{T}_{b,x}\left(z - z_0\right) + \hat{P}_b\right].\end{aligned} \tag{27}$$

The new set of governing equations is derived by substituting all stress and strain expressions Eqs. (15), (20a), (20b), (26) and (27) into Eq. (25) and setting the first variation to zero. The corresponding Euler-Lagrange field equations in terms of the functional unknowns $\lambda_1(x)$, $\lambda_2(x)$ and $\mathcal{F}$ are,

$$\delta\lambda_1 :\ N_{,x} + \hat{T}_t - \hat{T}_b = 0 \tag{28a}$$

$$\delta\lambda_2 :\ M_{,xx} + z_N\hat{T}_{t,x} - z_0\hat{T}_{b,x} + \hat{P}_t - \hat{P}_b = 0 \tag{28b}$$

$$\begin{aligned}&\delta\mathcal{F}^T :\ \left(\boldsymbol{s} + \boldsymbol{\eta}^s + \boldsymbol{\eta}^n\right)\mathcal{F} + \left(\boldsymbol{\eta}_x^s + \boldsymbol{\eta}_x^n\right)\mathcal{F}_{,x} + \left(\boldsymbol{\eta}_{xx}^s + \boldsymbol{\eta}_{xx}^n\right)\mathcal{F}_{,xx} + \boldsymbol{\eta}_{xxx}^n\mathcal{F}_{,xxx} + \boldsymbol{\eta}_{xxxx}^n\mathcal{F}_{,xxxx} +\\ &\hat{T}_b\boldsymbol{\chi}^s + \hat{T}_{b,x}\left(\boldsymbol{\chi}_x^s + \boldsymbol{\chi}_x^n\right) + \hat{T}_{b,xx}\boldsymbol{\chi}_{xx}^n + \hat{T}_{b,xxx}\boldsymbol{\chi}_{xxx}^n + \hat{P}_b\boldsymbol{\omega}^n + \hat{P}_{b,x}\boldsymbol{\omega}_x^n + \hat{P}_{b,xx}\boldsymbol{\omega}_{xx}^n + \boldsymbol{\Lambda}_{eq} = \boldsymbol{0}.\end{aligned} \tag{28c}$$

The pertinent essential and natural boundary conditions are given by,

$$\begin{aligned}\delta\mathcal{F}^T = 0 \quad \text{or} \quad &\left(\boldsymbol{\eta}^{sbc} + \boldsymbol{\eta}^{nbc}\right)\mathcal{F} + \left(\boldsymbol{\eta}_x^{sbc} + \boldsymbol{\eta}_x^{nbc}\right)\mathcal{F}_{,x} + \boldsymbol{\eta}_{xx}^{nbc}\mathcal{F}_{,xx} + \boldsymbol{\eta}_{xxx}^{nbc}\mathcal{F}_{,xxx} +\\ &\hat{T}_b\boldsymbol{\chi}^{sbc} + \hat{T}_{b,x}\boldsymbol{\chi}_x^{nbc} + \hat{T}_{b,xx}\boldsymbol{\chi}_{xx}^{nbc} + \hat{P}_b\boldsymbol{\omega}^{nbc} + \hat{P}_{b,x}\boldsymbol{\omega}_x^{nbc} + \boldsymbol{\Lambda}_{bc_1} = \hat{\mathcal{U}}_{bc}\end{aligned} \tag{29a}$$

$$\delta\mathcal{F}_{,x}^T = 0 \quad \text{or} \quad \boldsymbol{\rho}^{nbc}\mathcal{F} + \boldsymbol{\rho}_x^{nbc}\mathcal{F}_{,x} + \boldsymbol{\rho}_{xx}^{nbc}\mathcal{F}_{,xx} + \hat{T}_{b,x}\boldsymbol{\gamma}_x^{nbc} + \hat{P}_b\boldsymbol{\mu}^{nbc} + \boldsymbol{\Lambda}_{bc_2} = \hat{\mathcal{W}}. \tag{29b}$$

The governing equations related to δF^T are written in matrix notation, with each row defining a separate equation. Eqs. (28c) are enhanced versions of the CLA constitutive equation $M = Dw_{,xx}$, taking into account transverse shearing and transverse normal effects, and the influence of the higher-order moments. The members of $\boldsymbol{\eta}$ are correction factors related to either transverse shear stresses

(superscript s) or transverse normal stresses (superscript n). The addition of the superscript bc to s and n denote correction factors for the boundary equations. Similarly, members of row vectors $\boldsymbol{\chi}$ and $\boldsymbol{\omega}$ are correction factors related to the surface shear and normal tractions, respectively. The terms $\boldsymbol{\rho}$, $\boldsymbol{\gamma}$ and $\boldsymbol{\mu}$ in the second set of boundary equations $\delta\mathcal{F}^T_{,x}$ stem only from transverse normal stresses. Column vectors $\boldsymbol{\Lambda}$ only include the Lagrange multipliers λ_1, λ_2 and their derivatives.

The full derivation of the governing equations including details of all coefficients are given in the Appendix. Finally, the expressions found in Eq. (29a) is used to determine the deformation vector $\mathcal{U}$ of the reference surface, whereas the second row of Eq. (29b) is used to find an expression for the bending deflection w throughout the entire domain.

2.2 Differential quadrature method

In this work the governing equations (28) and associated boundary conditions (29) are solved in their strong form using a numerical technique known as the Differential Quadrature Method (DQM). DQM has been shown to be an efficient and robust solution technique for solving both stretching and bending [34] and stability problems [35] of variable stiffness composites.

In DQM a derivative of a funtion at a grid point is calculated from a linear weighted sum of all the functional values within the grid, i.e.

$$\frac{\mathrm{d}^n f(x_i)}{\mathrm{d}x^n} = \sum_{i=1}^{N} A_{ij}^{(n)} f(x_j) \tag{30}$$

where n is the order of the derivative, N is the number of gridpoints and $\boldsymbol{A}^{(n)}$ is the DQ weighting matrix for the n^{th} derivative. The weighting matrix can be derived using different polynomial assumptions as a basis but here the Lagrangian polynomial weighting matrix of the Generalised DQM [36] based on a non-uniform Chebychev-Gauss-Lobatto grid is used. In this manner each differential operator in the differential equations is replaced by a matrix operator, such that the differential equations are converted to algebraic ones that are solved by standard linear algebra operations.

3 RESULTS

The Hellinger-Reissner model derived above is applied to a number of variable stiffness and straight fibre laminated beams subjected to bending. A plane strain assumption in the lateral y-direction is invoked such that the results are also valid for an infinitely wide plate. Initial numerical studies revealed that a third-order model with zig-zag functionality is sufficient to capture the higher-order effects relevant for the laminates investigated. Even though the zig-zag moments do not contribute significantly toward the results for laminates modelled in this study, they are nevertheless important for accurately modelling boundary layers in the stress fields close to clamped boundaries.

For simplicity only two boundary conditions, both ends simply-supported (SS) or both ends clamped (CC), are analysed in this report. Upon validation, the model is implemented in an optimisation scheme to tailor the through-thickness stress field in order to delay the onset of delaminations. All beams considered are 250 mm long and subjected to uniform normal tractions of $\bar{P}_t = -50$ kPa on the top surface and $\bar{P}_b = 50$ kPa on the bottom surface to induce a total pressure loading of $p_0 = 100$ kPa in one direction.

3.1 3D stress-field validation

A third-order zig-zag Hellinger-Reissner formulation for straight-fibre laminates has been extensively validated against 3D elasticity solutions [32]. As the formulation is extended here to variable stiffness beams, initial validation of the theory is required. To the authors' knowledge there are no closed form 3D elasticity solutions for variable stiffness beams, therefore high-fidelity 3D finite element models are used to correlate the full 3D stress field and bending deflection.

Variable stiffness beams with linear fibre angle variations in the spanwise direction of each ply are defined using the notation by Gurdal & Olmedo [37],

$$\alpha(x) = \frac{2(T_1 - T_0)}{L}|x| + T_0 \quad \text{written as} \quad \langle T_0|T_1\rangle \tag{31}$$

where $\alpha(x)$ is the local fibre angle at co-ordinate x, and T_0 and T_1 are the fibre angles at the beam midspan $x = 0$ and ends $x = \pm L/2$, respectively. Table 1 below summarises two variable stiffness layups that are analysed using the CC and SS boundary conditions. The material properties chosen are those of IM7-8552 and are summarised in Table 2.

Laminate	Layup	t_{ply} (mm)
A	$[\langle 90\|0\rangle/\langle -90\|0\rangle/\langle 45\| -45\rangle/\langle -45\|45\rangle]_s$	1.5625
B	$[\langle 90\|20\rangle/\langle 45\| -25\rangle/\langle -90\| -20\rangle/\langle -45\|25\rangle]_s$	1.5625

Table 1: Stacking sequences and material properties of two variable stiffness laminates used to validate the present model against 3D finite element solutions

E_{11}	E_{22}	E_{33}	υ_{12}	υ_{13}	υ_{23}	G_{12}	G_{13}	G_{23}
163 GPa	12 GPa	12 GPa	0.3	0.3	0.3	5 GPa	4 GPa	3.2 GPa

Table 2: Mechanical properties of IM7-8552 assumed throughout this paper

Figures 1-8 compare the bending deflection, normalised axial stress $\bar{\sigma}_x$, normalised transverse shear stress $\bar{\tau}_{xz}$ and normalised transverse normal stress $\bar{\sigma}_z$ for Laminates A and B in Table 1 against 3D FEM results for the two boundary conditions CC and SS. The normalised quantities are defined as follows,

$$\bar{w} = \frac{10^6 t^2}{p_0 L^4} \int_{-\frac{t}{2}}^{\frac{t}{2}} u_z(x,z)\,\mathrm{d}z, \quad \bar{\sigma}_x = \frac{t^2}{p_0 L^2}\cdot\sigma_x(x,z), \quad \bar{\tau}_{xz} = \frac{1}{p_0}\cdot\tau_{xz}(x,z), \quad \bar{\sigma}_z = \frac{1}{p_0}\cdot\sigma_z(x,z). \tag{32}$$

The 3D FEM model in Abaqus features a 250 mm long (x-direction), 1000 mm wide (y-direction) and 12.5 mm thick (z-direction) plate that is meshed using a total of 95,880 C3D8R elements with 799 elements in the x-direction, 120 elements in the z-direction, i.e. 15 elements per ply, and a single element in the y-direction. The plane strain condition in the y-direction is enforced by the high width-to-length aspect ratio, the use of a single element in the y-direction and boundary conditions that prevent the shorter sides from expanding laterally. In Figures 1-8 the in-plane stress $\bar{\sigma}_x$ and transverse normal stress $\bar{\sigma}_z$ through-thickness distributions are plotted at mid-span ($x = 0$) while the transverse shear stress is plotted at quarter-span ($x = -L/4$).

All figures show good correlation between the 3D FEM results and the present third-order zig-zag Hellinger-Reissner model. The correlation between the results is not as good as in the case of straight-fibre laminates investigated in [32], where a closed form 3D elasticity solution was available for validation purposes. In the 3D FEM analysis the structural problem is solved in the weak form and the linear interpolation of the elements means that all variables are C^0-continuous, which may lead to inaccuracies in the computation of derivatives, i.e. strains, and by extension, stresses. In all cases the axial stress σ_x and transverse shear stress τ_{xz} are well correlated while the transverse normal stress σ_z features the most discrepancies between 3D FEM and the present model. However, for the laminates investigated in this study the magnitude of σ_z is at least an order of magnitude lower than σ_x or τ_{xz} and therefore does not play a big role in the initiation of delaminations that is investigated in Section 3.2.

It is worth noting that the plot of transverse shear stress in Figure 4a shows both negative and positive values throughout the thickness. In isotropic beams and all straight-fibre laminates known to the authors the beam cross-section is sheared in one direction only. In this variable stiffness case on the other hand the center of the beam is sheared in the opposite direction to the surface layers. The mechanism behind this phenomenon is beyond the scope of this report but will be analysed in future work.

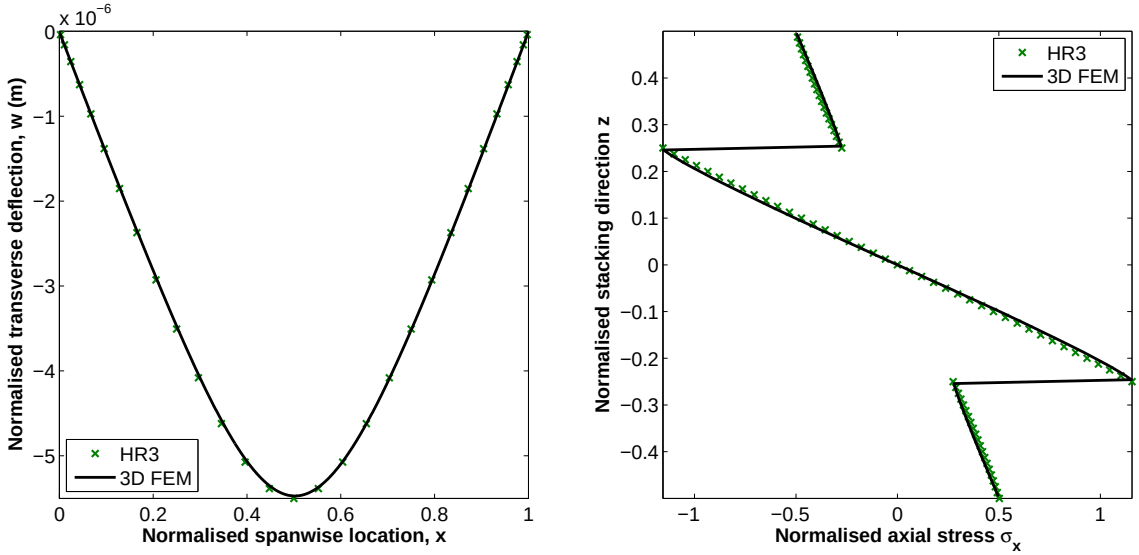

(a) Normalised transverse displacement, $\bar{w}$ (b) Normalised in-plane stress, $\bar{\sigma}_x$

Figure 1: Laminate A boundary condition SS: Normalised bending displacement and through-thickness distribution of the normalised in-plane stress (at $x = 0$)

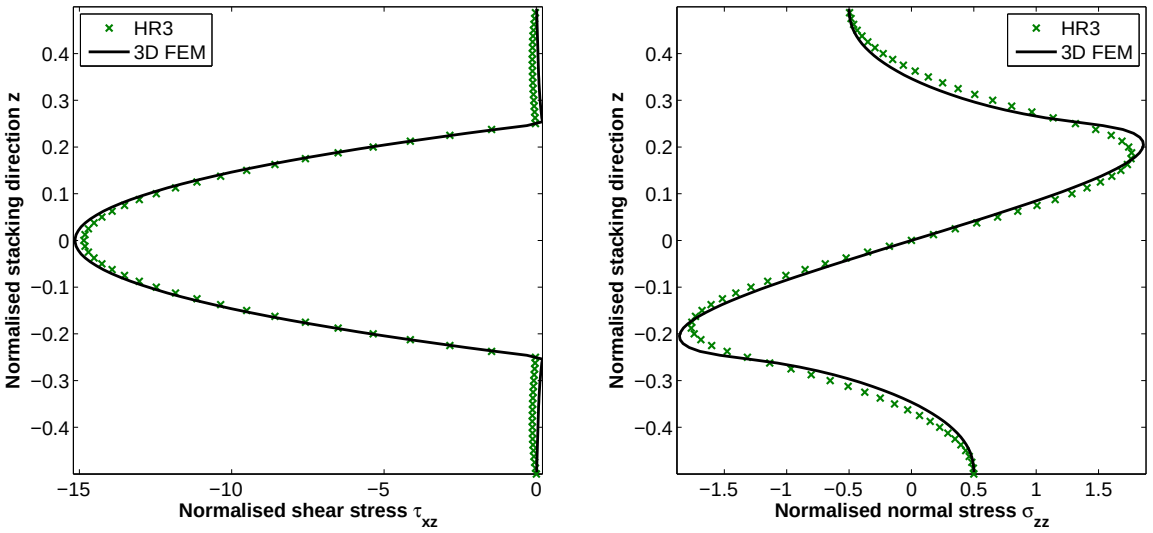

(a) Normalised transverse shear stress, $\bar{\tau}_{xz}$ (b) Normalised transverse normal stress stress, $\bar{\sigma}_z$

Figure 2: Laminate A boundary condition SS: Through-thickness distribution of the normalised transverse shear stress (at $x = -L/4$) and normalised transverse normal stress (at $x = 0$)

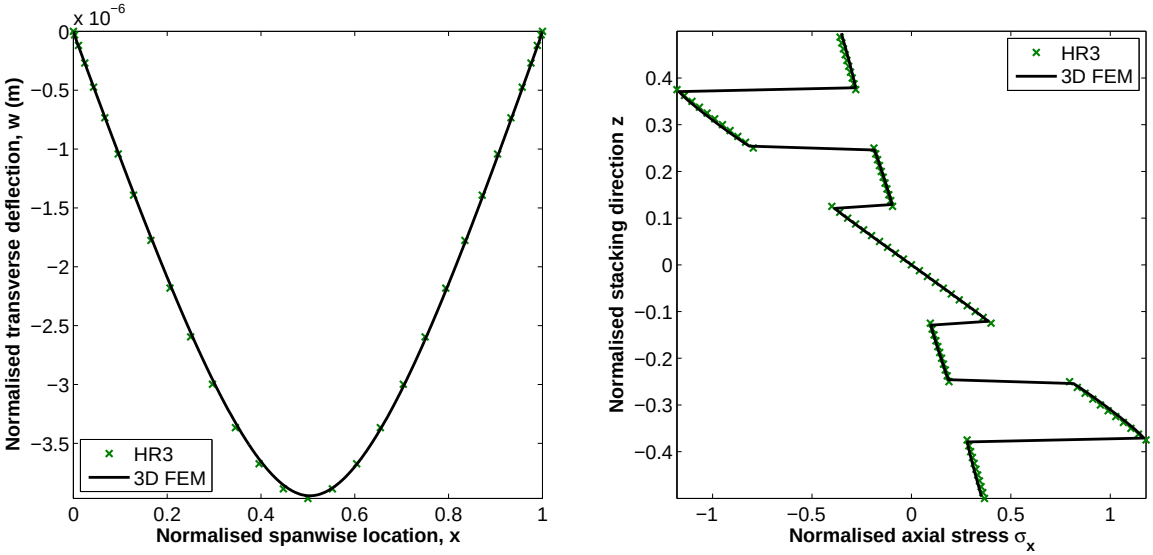

(a) Normalised transverse displacement, $\bar{w}$

(b) Normalised in-plane stress, $\bar{\sigma}_x$

Figure 3: Laminate B boundary condition SS: Normalised bending displacement and through-thickness distribution of the normalised in-plane stress (at $x = 0$)

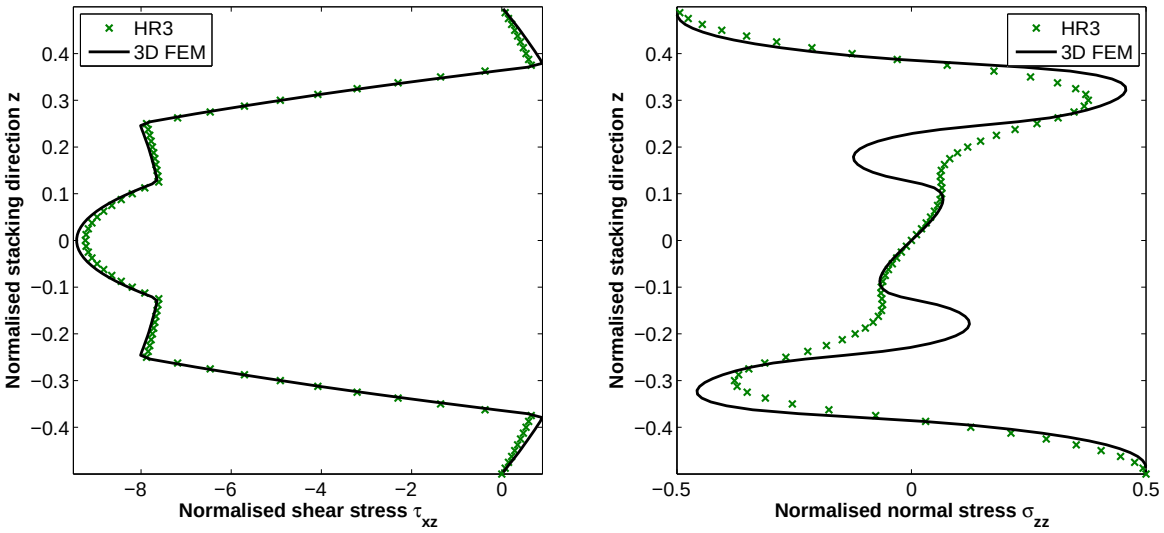

(a) Normalised transverse shear stress, $\bar{\tau}_{xz}$

(b) Normalised transverse normal stress stress, $\bar{\sigma}_z$

Figure 4: Laminate B boundary condition SS: Through-thickness distribution of the normalised transverse shear stress (at $x = -L/4$) and normalised transverse normal stress (at $x = 0$)

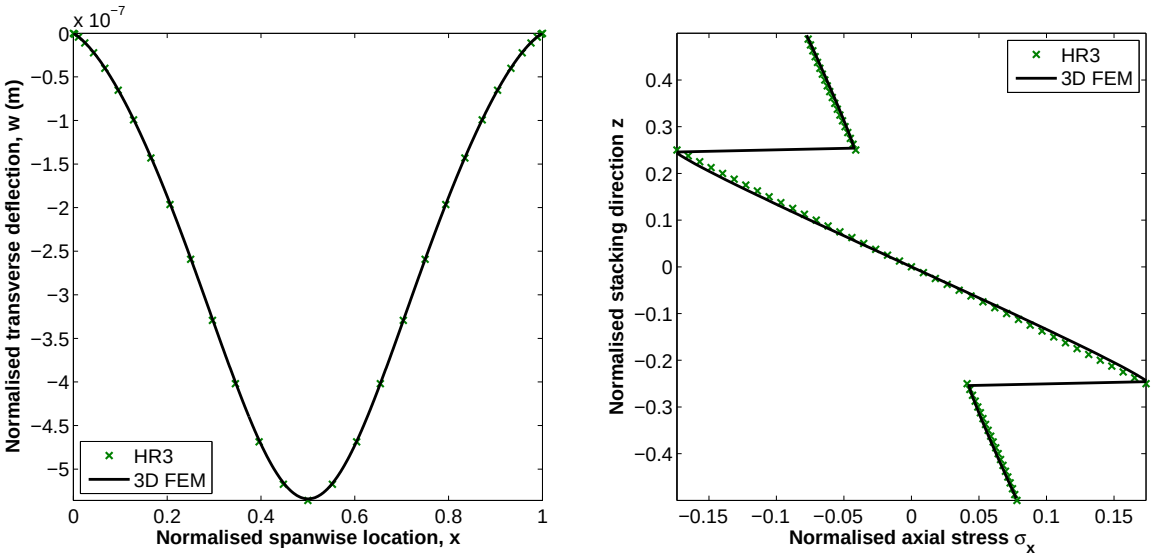

(a) Normalised transverse displacement, $\bar{w}$

(b) Normalised in-plane stress, $\bar{\sigma}_x$

Figure 5: Laminate A boundary condition CC: Normalised bending displacement and through-thickness distribution of the normalised in-plane stress (at $x = 0$)

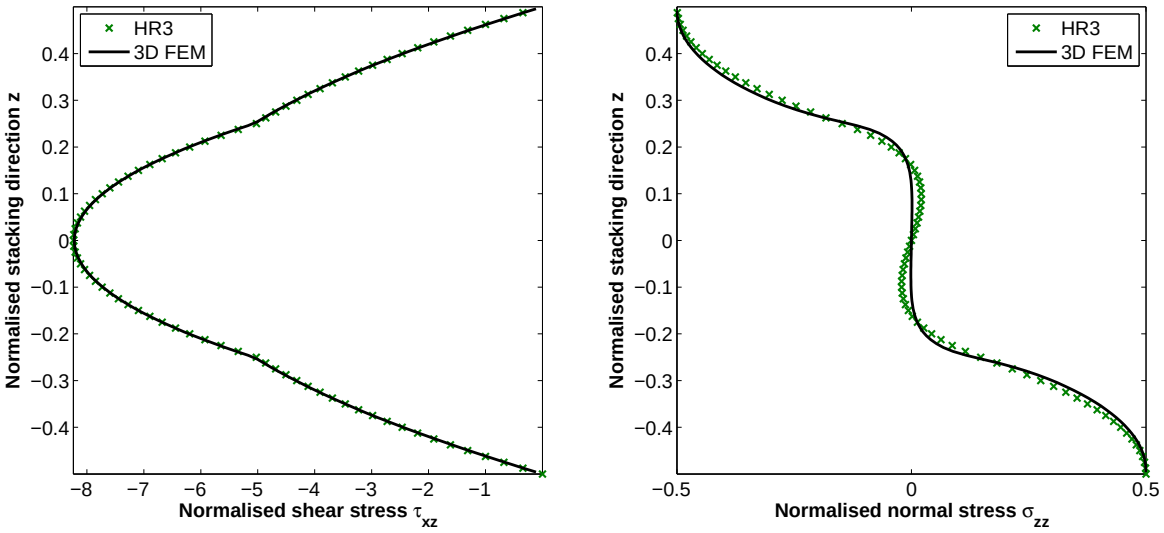

(a) Normalised transverse shear stress, $\bar{\tau}_{xz}$

(b) Normalised transverse normal stress stress, $\bar{\sigma}_z$

Figure 6: Laminate A boundary condition CC: Through-thickness distribution of the normalised transverse shear stress (at $x = -L/4$) and normalised transverse normal stress (at $x = 0$)

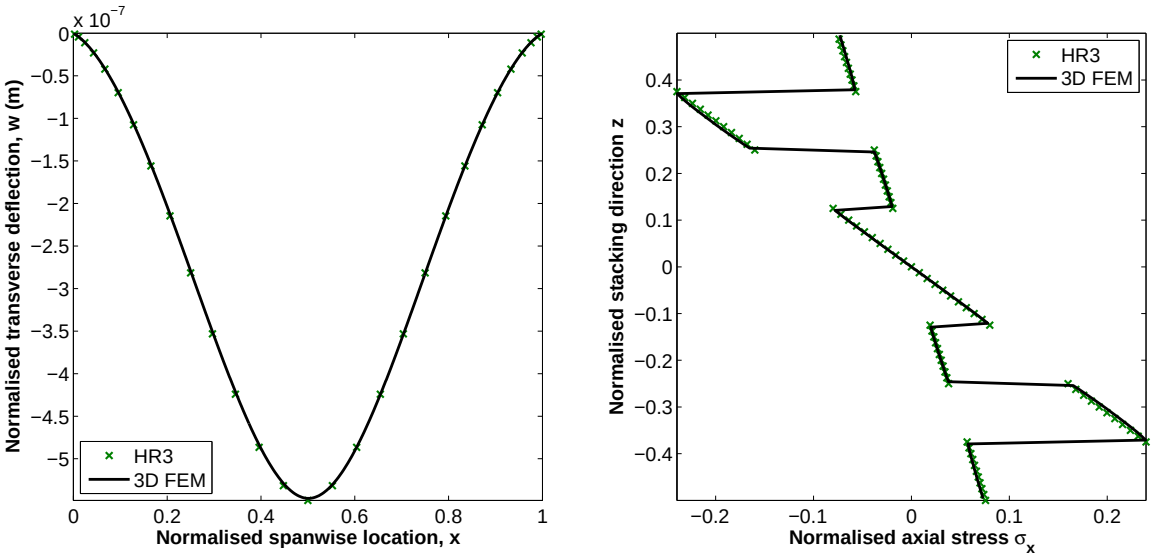

(a) Normalised transverse displacement, $\bar{w}$

(b) Normalised in-plane stress, $\bar{\sigma}_x$

Figure 7: Laminate B boundary condition CC: Bending displacement and through-thickness distribution of the normalised in-plane stress (at $x = 0$)

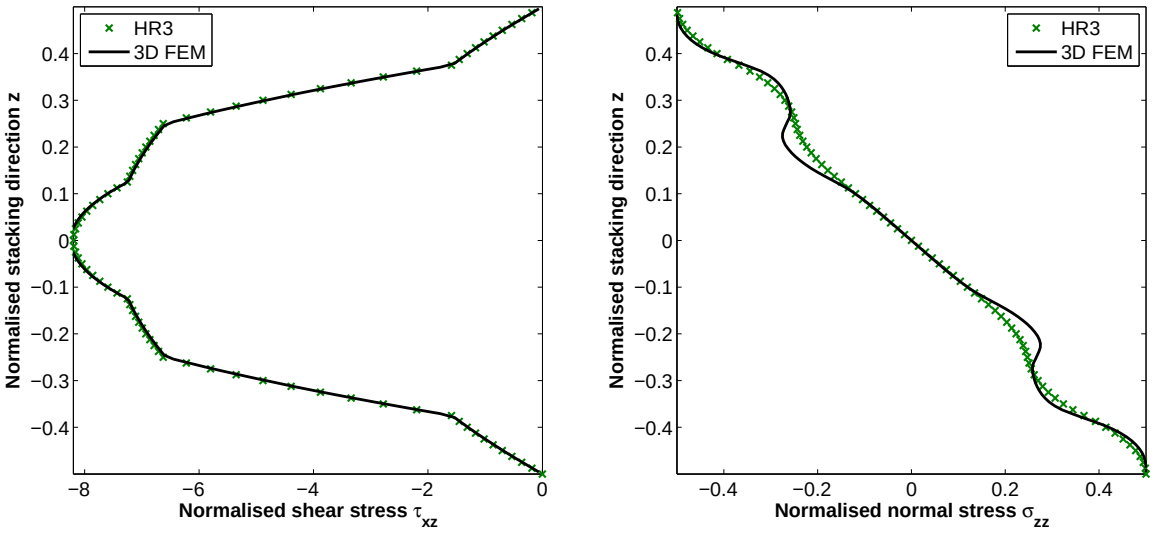

(a) Normalised transverse shear stress, $\bar{\tau}_{xz}$

(b) Normalised transverse normal stress stress, $\bar{\sigma}_z$

Figure 8: Laminate B boundary condition CC: Through-thickness distribution of the normalised transverse shear stress (at $x = -L/4$) and normalised transverse normal stress (at $x = 0$)

3.2 Transverse stress-field tailoring

The aim of this work is to take advantage of variable fibre angle technology to tailor the through-thickness stress distributions of the transverse shear and normal stresses. A popular metric for predicting the onset of delamination in layered composites is the quadratic failure criterion of Camanho et al. [38]

$$f = \left(\frac{\langle \sigma_{zz} \rangle}{N}\right)^2 + \left(\frac{\tau_{xz}}{S}\right)^2 + \left(\frac{\tau_{yz}}{T}\right)^2 \tag{33}$$

where N is the interlaminar tensile strength, and S and T are the interlaminar shear strengths. Delamination initiation is assumed to occur when $f \geq 1$. Macaulay brackets $\langle\rangle$[1] are used because compressive transverse normal stresses do not contribute to the initiation of delaminations. In the beam problem considered here $\tau_{yz} = 0$ such that delamination initiation is driven by σ_{zz} and τ_{xz} at the interface between two plies with different material properties, which are calculated using Eqs. (20a) and (20b). In this respect variable stiffness composites can be used to reach a compromise between maintaining high overall bending stiffness and reducing local interfacial stress concentrations.

3.2.1 Analytical example

Consider the problem of a simply-supported, four-layer cross-ply beam in bending loaded by a uniform pressure on the top surface. Depending on the arrangement of the four layers the transverse shear stress profile is dramatically changed. Figure 9 compares the transverse shear stress profile at the support $x = -L/2$ through the thickness of a $[0/90]_s$ and a $[90/0]_s$ laminate. For both laminates the maximum shear stress occurs at the mid-plane and the shear stress vanishes at both surfaces due to the absence of external shear tractions. Fundamental beam theory states that the shear force, i.e. the integral of the transverse shear stress through the thickness, is independent of the layup and only depends on the loading condition. Based on these two insights it is apparent that in order to distribute stresses most evenly the shear stress should increase as rapidly as possible away from the outer surfaces and then remain constant for the rest of the crossection. In the ideal case the entire cross-section is sheared by the same amount, thereby spreading load equally and minimising the shear stress amplitude.

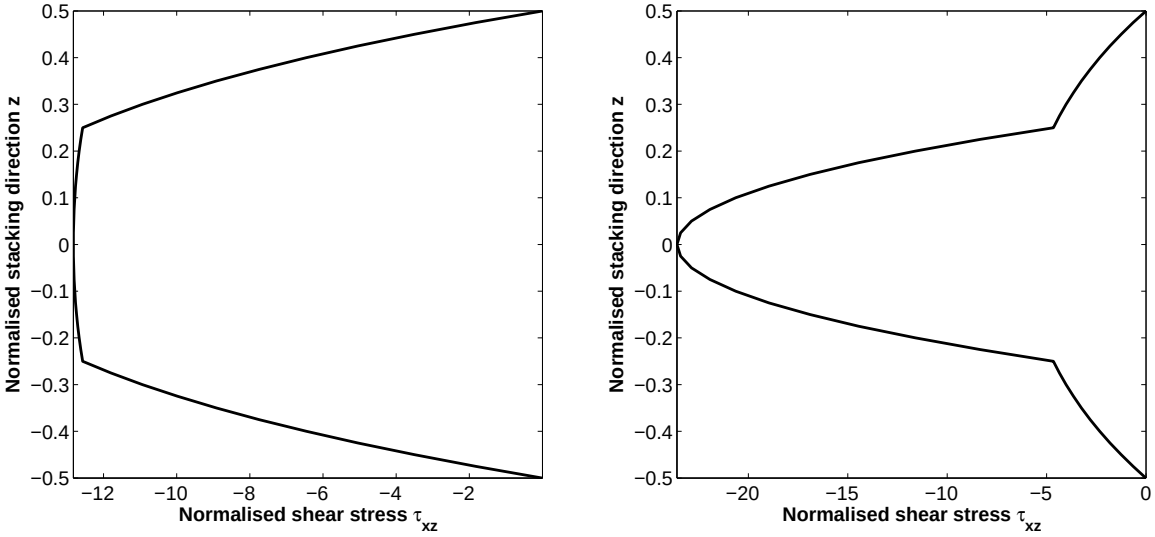

(a) $[0/90/90/0]_s$

(b) $[90/0/0/90]_s$

Figure 9: Through-thickness distribution of normalised transverse shear stress (at $x = -L/2$) for two cross-ply laminates

[1] $\langle x \rangle = 0$ for $x \leq 0$ and $\langle x \rangle = x$ for $x > 0$

Due to the greater axial and transverse shear rigidity of the 0° layers this scenario can be realised by placing the stiffer 0° on the outside and using the less stiff 90° layers as a core. In the opposite case the transverse shear stress remains close to zero in the outer 90° layers causing a local stress concentration in the central 0° layers with an overall greater shear stress magnitude.

Even for such a simple scenario the two cases present a non-trivial tradeoff. The $[0/90]_s$ laminate maximises bending stiffness and reduces the maximum shear stress magnitude throughout the thickness by placing the stiffer 0° towards the surfaces. Conversely, the $[90/0]_s$ laminate significantly reduces the shear stress at the interface between the 0° and 90° layers that is a critical factor in driving delamination initiation. Thus, a compromise needs to be reached between minimising bending deflection and reducing the chance of intraply transverse shear cracking, or minimising delaminations.

This tradeoff ultimately depends on the structural requirements and material strengths being considered and is not only restricted to this illustrative case of a cross-ply laminate. To an extent a similar phenomenon occurs for a quasi-isotropic laminate, whereby a $[\pm 45/90/0]_s$ stacking sequence is comparable to the $[90/0]_s$ laminate, while a $[0/\pm 45/90]$ stacking sequence is the analog to the $[0/90]_s$ laminate.

3.2.2 Numerical example

An optimisation study was conducted to ascertain if beams manufactured using composite plies with variable fibre angles could

1. Reduce the likelihood of delaminations compared to an optimised straight-fibre, quasi-isotropic beam, i.e. reduce the maximum value of the initiation criterion f in Eq. (33) at the interfaces between plies with different material properties
2. Find a compromise between maximising overall bending rigidity and minimising the likelihood of delaminations

For both opimisation studies above a 250 mm long and 16 mm thick beam with either SS or CC boundary conditions was analysed, i.e. a total of four optimisation studies 1-CC, 1-SS, 2-SS and 2-CC. The material properties are defined in Table 2 and the interlaminar strengths are $N = 99$ MPa and $S = 113$ MPa. Initially the 16-ply quasi-isotropic, balanced and symmetric baseline design comprised of straight-fibre $\pm 45^\circ, 0^\circ$ or 90° plies is sought for each optimisation case. For example, in the $[45, -45, 0, 90, 0, 90, -45, 45]_s$ stacking sequence each fibre angle represents a stack of four 0.25 mm plies within which delaminations cannot occur. Thus, the goal is to re-arrange the ply blocks such as to minimise the appropriate fitness function.

For the variable stiffness designs the laminate is constrained to the balanced and symmetric form $[\pm\langle T_0^1|T_1^1\rangle, \cdots, \pm\langle T_0^8|T_1^8\rangle]_s$. There are 32 blocks of variable stiffness layers each comprised of two 0.25 mm IM7-8552 plies such that each $\pm$ pair of variable stiffness plies is equivalent to a stack of four straight-fibre plies in the quasi-isotropic baseline designs.

For the variable stiffness laminates the two optimisation problems are formulated as follows

$$\begin{aligned} &1) \quad \text{Minimise:} && \max\{f(\boldsymbol{v})\} \\ &2) \quad \text{Minimise:} && \max\{f(\boldsymbol{v})\} \cdot \max\{w(\boldsymbol{v})\} \\ &\qquad \text{Variables:} && \boldsymbol{v}: \quad \begin{bmatrix} T_0^1 & \dots & T_0^8 & T_1^1 & \dots & T_1^8 \end{bmatrix} \\ &\qquad \text{Subject to:} && 0^\circ \leq T_s^k \leq 90^\circ \quad (s = 0, 1 \text{ and } k = 1 \dots 8). \end{aligned} \tag{34}$$

The delamination initiation factor f of Eq. (33) is calculated at the top and bottom of each ply, i.e. the interfaces, and at all DQ grid points x_i throughout the grid.

The optimisation problem is solved using a genetic algorithm (GA) in the commercial software package MATLAB. The crossover probability is chosen to be 0.8 and the children of future generations are created using a weighted average of the parents. The mutation function is a MATLAB adaptive-feasible algorithm that creates random changes in the population individuals with the direction and step length adaptive to the prior successful or unsuccessful generation. Due to the large number of design variables and the non-convexity of the optimisation problem the convergence of the GA is relatively slow and a global minimum is not guaranteed. To improve the convergence rate a hybrid optimisation scheme is implemented whereby the GA is used to find the region near an optimum point after only a small number of generations, typically less than 20, and a pattern-search

algorithm is then used for a faster and more efficient local search. To prevent entrapment in local minima a variety of random and specific initial seed populations are tested, with the range of individuals in the initial population set to include the whole design space $T_s^k \in [0°, 90°]$ and the population size set to 15-20 times the number of design variables.

Optimisation	Layup	Fit. Function	Change
1 - SS	$[0_2/45/-45/90_2/-45/45]_s$	7.10×10^{-3}	-
	$[0_2/\pm\langle 90\|71\rangle/\pm\langle 90\|84\rangle/90_4/$ $\pm\langle 81\|89\rangle/\pm\langle 0\|83\rangle/\pm\langle 0\|77\rangle]_s$	6.20×10^{-3}	-12.6%
1 - CC	$[0/45/90/-45/90/45/-45/0]_s$	5.91×10^{-3}	-
	$[\pm\langle 70\|10\rangle/\pm\langle 2\|73\rangle/\pm\langle 10\|74\rangle/\pm\langle 34\|66\rangle/$ $\pm\langle 82\|85\rangle/\pm\langle 41\|48\rangle/\pm\langle 4\|65\rangle/\pm\langle 0\|17\rangle]_s$	5.47×10^{-3}	-7.4%
2 - SS	$[0_2/45/-45/45/90/90/-45]_s$	1.05×10^{-5}	-
	$[0_4/\pm\langle 0\|62\rangle/\pm\langle 0\|72\rangle/\pm\langle 0\|76\rangle_3/\pm\langle 0\|71\rangle]_s$	7.82×10^{-6}	-25.3%
2 - CC	$[0/-45/0/90/45/-45/90/45]_s$	2.93×10^{-6}	-
	$[0_2/\pm\langle 0\|3\rangle/\pm\langle 0\|35\rangle/\pm\langle 0\|26\rangle/$ $\pm\langle 0\|9\rangle/\pm\langle 0\|3\rangle/0_4]_s$	2.26×10^{-6}	-22.8%

Table 3: Optimised straight-fibre and variable stiffness laminates with associated value of the fitness function. The percentage change indicates the reduction in fitness function magnitude of the variable stiffness designs compared to the straight-fibre designs.

Table 3 summarises the optimised straight-fibre and variable stiffness laminates found using the GA for the four optimisation studies. In all cases the variable stiffness designs improve upon the optimal straight-fibre designs. The structural mechanism behind the improvements is readily explained by example of case 2-SS. Fundamental beam theory states that the maximum transverse shear force must occur at the supports for a simply-supported beam loaded by a uniformly distributed load. Furthermore, the stiffness of the beam can be reduced over the supports as the transverse deflection is constrained. To reduce the likelihood of delaminations in this area the magnitude of the maximum transverse shear stress can be minimised using the mechanism previously described in Figure 9a, i.e. stiffer layers towards the surfaces with a softer core. In the optimial design for case 2 - SS the local layup above the supports is $[0_4/\pm 62/\pm 72/\pm 76_3 \pm 71]_s$ which agrees with the above qualitative explanation. Furthermore, the layup at the centre of the beam, i.e. the point of maximum bending deflection, is $[0_{32}]$ which gives the maximum possible bending stiffness. Compared to the quasi-isotropic design the variable stiffness laminates therefore have the capability to increase bending stiffness towards unsupported areas, while optimising the layup for distributing transverse stresses at supported areas where stress concentrations are more likely. Overall this results in decreased bending deflection and a reduction in the peak transverse shear stress as shown in Figure 10. This figure also shows that the variable stiffness design reduces the peak bending displacement more than the peak transverse shear stress, which explains why the fitness function in Table 3 is improved more for case 2 (bending and delamination) than for case 1 (delamination only).

4 CONCLUSIONS

In this paper a higher-order zig-zag theory derived from the Hellinger-Reissner mixed variational principle was presented for the stretching and bending of highly heterogeneous, laminated, variable stiffness beams. The model was used to analyse the bending of variable stiffness beams under simply-supported and clamped boundary conditions and the full 3D stress field validated against 3D finite element results. The correlation in this paper was not as good as against 3D elasticity solutions for straight-fibre laminates previously presented in [32]. However, this is believed to be due to the weak formulation and linear interpolation of the FEM which can lead to inaccuracies in the computation of derivatives, i.e. strains and stresses.

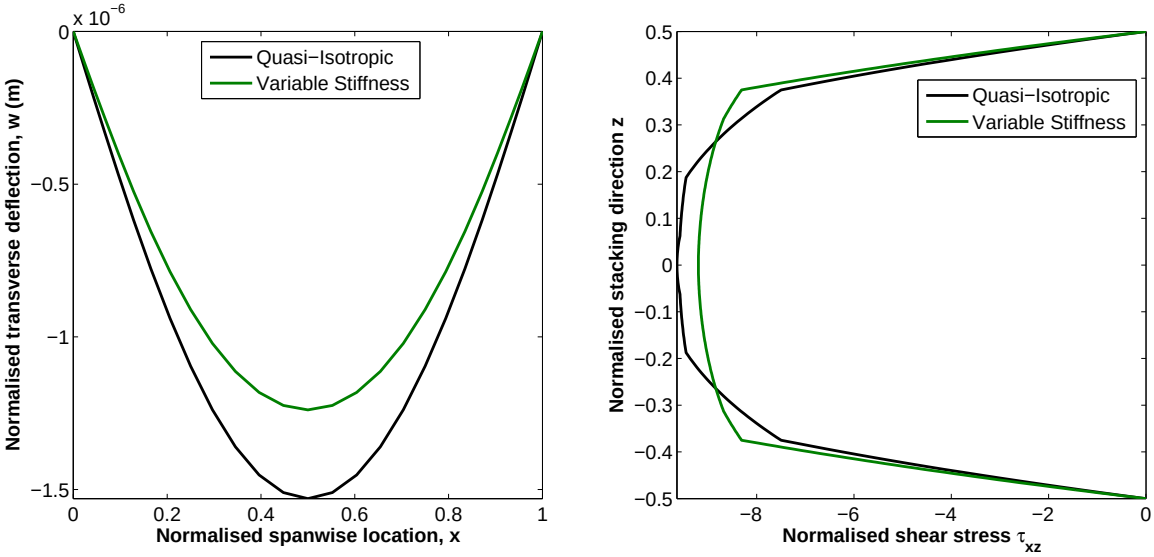

(a) $\bar{w}$ (b) $\bar{\tau}_{xz}$ at $x = -L/2$

Figure 10: Case 2 - SS: Comparison of bending deflection $\bar{w}$ and through-thickness profile of transverse shear stress $\bar{\tau}_{xz}$ at the support $x = -L/2$ for quasi-isotropic and variable stiffness optimal designs.

The present model was then used to minimise the likelihood of delaminations in laminates with blocked plies. Furthermore, a second optimisation study intended to find a compromise between achieving high bending stiffness and reducing the likelihood of delaminations. The findings showed that variable stiffness laminates provide significant improvements over baseline quasi-isotropic design. For straight-fibre laminates the transverse shear and transverse normal stresses are functions of the local material properties and the derivatives of the functional unknowns. In the case of variable stiffness laminates the derivatives of the material properties also influence the magnitude and through-thickness distribution of the transverse stresses, and therefore provide more design freedom to tailor the 3D stress field. Furthermore, variable stiffness laminates can be designed to guarantee high global bending stiffness while locally tailoring the 3D stress-field at areas of stress-concentration. In this regard variable stiffness laminates offer the promising opportunity of simultaneously tailoring the global and local structural behaviour.

A Derivation of HR Governing Equations

The Hellinger-Reissner function in Eq. (25) can be split into separate components representing the potential of axial stress Π_{σ_x}, transverse shear stress $\Pi_{\tau_{xz}}$ and transverse normal Π_{σ_z} stress, the potential of boundary tractions Π_Γ and the potential of the Lagrange multiplier constraints Π_λ. Substituting the pertinent expressions for stresses and strains into the functional of Eq. (25) yields,

$$\delta\Pi = \delta\left(\Pi_{\sigma_x} + \Pi_{\tau_{xz}} + \Pi_{\sigma_z} + \Pi_\lambda + \Pi_\Gamma\right) = 0$$

$$\Pi_{\sigma_x} = \frac{1}{2}\int_V \sigma_x^T \epsilon_x \mathrm{d}V = \frac{1}{2}\int_V \mathcal{F}^T \boldsymbol{s}^T \boldsymbol{f}^{(k)^T} \bar{Q}^{(k)} \boldsymbol{f}^{(k)} \boldsymbol{s}\mathcal{F}\mathrm{d}V \tag{35a}$$

$$\Pi_{\tau_{xz}} = \frac{1}{2}\int_V \tau_{xz}^T \gamma_{xz}\mathrm{d}V = \frac{1}{2}\int_V \left[\frac{\mathrm{d}}{\mathrm{d}x}\left\{\boldsymbol{c}^{(k)}\boldsymbol{s}\mathcal{F}\right\} + \hat{T}_b\right]^T \frac{1}{G_{xz}^{(k)}}\left[\frac{\mathrm{d}}{\mathrm{d}x}\left\{\boldsymbol{c}^{(k)}\boldsymbol{s}\mathcal{F}\right\} + \hat{T}_b\right]\mathrm{d}V \tag{35b}$$

$$\Pi_{\sigma_z} = \frac{1}{2}\int_V \sigma_z^T \epsilon_z \mathrm{d}V = \frac{1}{2}\int_V \left[\frac{\mathrm{d}^2}{\mathrm{d}x^2}\left\{\boldsymbol{e}^{(k)}\boldsymbol{s}\mathcal{F}\right\} - \hat{T}_{b,x}\left(z - z_0\right) + \hat{P}_b\right\}^T \cdot$$
$$\left[R_{13}^{(k)}\bar{Q}^{(k)}\boldsymbol{f}^{(k)}\boldsymbol{s}\mathcal{F} + R_{33}^{(k)}\left\{\frac{\mathrm{d}^2}{\mathrm{d}x^2}\left(\boldsymbol{e}^{(k)}\boldsymbol{s}\mathcal{F}\right) - \hat{T}_{b,x}\left(z - z_0\right) + \hat{P}_b\right\}\right]\mathrm{d}V \tag{35c}$$

$$\Pi_\lambda = \int \lambda_1 \left(N_{,x} + \hat{T}_t - \hat{T}_b \right) \mathrm{d}x + \int \lambda_2 \left(M_{,xx} + z_N \hat{T}_{t,x} - z_0 \hat{T}_{b,x} + \hat{P}_t - \hat{P}_b \right) \mathrm{d}x \tag{35d}$$

$$\Pi_\Gamma = -\int_{S_2} \left(\sigma_x \hat{u}_x^{(k)} + \tau_{xz} \hat{w} \right) \mathrm{d}S_2 = -\int \left[\sigma_x \begin{bmatrix} \boldsymbol{f}_g^{(k)} & \phi^{(k)} \end{bmatrix} \begin{pmatrix} \hat{\mathcal{U}}_g \\ \psi \end{pmatrix} + \tau_{xz} \hat{w} \right] \Bigg|_{x_A}^{x_B} \mathrm{d}z. \tag{35e}$$

Performing the variations on the functionals in Eqs. (35a)-(35e) following the rules of the calculus of variations results in the following expressions. For the potential of axial stress we have,

$$\begin{aligned} \delta\Pi_{\sigma_x} =& \delta \left\{ \frac{1}{2} \int \mathcal{F}^T \boldsymbol{s}^T \left(\int \boldsymbol{f}^{(k)^T} \bar{Q}^{(k)} \boldsymbol{f}^{(k)} \mathrm{d}z \right) \boldsymbol{s} \mathcal{F} \mathrm{d}x \right\} \\ =& \delta \left\{ \frac{1}{2} \int \mathcal{F}^T \boldsymbol{s}^T \boldsymbol{S} \boldsymbol{s} \mathcal{F} \mathrm{d}x \right\} = \delta \left\{ \frac{1}{2} \int \mathcal{F}^T \boldsymbol{s}^T \mathcal{F} \mathrm{d}x \right\} = \int \mathcal{F}^T \boldsymbol{s}^T \delta\mathcal{F} \mathrm{d}x. \end{aligned} \tag{36}$$

For the potential of transverse shear stress,

$$\begin{aligned} \delta\Pi_{\tau_{xz}} =& \delta \left\{ \frac{1}{2} \int_V \left[\frac{\mathrm{d}}{\mathrm{d}x} \left(\boldsymbol{c}^{(k)} \boldsymbol{s} \mathcal{F} \right)^T \frac{1}{G_{xz}^{(k)}} \frac{\mathrm{d}}{\mathrm{d}x} \left(\boldsymbol{c}^{(k)} \boldsymbol{s} \mathcal{F} \right) + 2 \frac{\hat{T}_b}{G_{xz}^{(k)}} \frac{\mathrm{d}}{\mathrm{d}x} \left(\boldsymbol{c}^{(k)} \boldsymbol{s} \mathcal{F} \right) + \frac{\hat{T}_b^2}{G_{xz}^{(k)}} \right] \mathrm{d}V \right\} \\ =& \int_V \left[\mathcal{F}^T \left\{ \left(\boldsymbol{c}^{(k)} \boldsymbol{s} \right)_{,x}^T \frac{1}{G_{xz}^{(k)}} \left(\boldsymbol{c}^{(k)} \boldsymbol{s} \right)_{,x} \right\} + \mathcal{F}_{,x}^T \left\{ \boldsymbol{s}^T \boldsymbol{c}^{(k)^T} \frac{1}{G_{xz}^{(k)}} \left(\boldsymbol{c}^{(k)} \boldsymbol{s} \right)_{,x} \right\} + \right. \\ & \left. \hat{T}_b \left\{ \frac{1}{G_{xz}^{(k)}} \left(\boldsymbol{c}^{(k)} \boldsymbol{s} \right)_{,x} \right\} \right] \delta\mathcal{F} \mathrm{d}V + \int_V \left[\mathcal{F}^T \left\{ \left(\boldsymbol{c}^{(k)} \boldsymbol{s} \right)_{,x}^T \frac{1}{G_{xz}^{(k)}} \boldsymbol{c}^{(k)} \boldsymbol{s} \right\} + \right. \\ & \left. \mathcal{F}_{,x}^T \left\{ \boldsymbol{s}^T \boldsymbol{c}^{(k)^T} \frac{1}{G_{xz}^{(k)}} \boldsymbol{c}^{(k)} \boldsymbol{s} \right\} + \hat{T}_b \left\{ \frac{1}{G_{xz}^{(k)}} \boldsymbol{c}^{(k)} \boldsymbol{s} \right\} \right] \delta\mathcal{F}_{,x} \mathrm{d}V. \end{aligned} \tag{37}$$

Performing integration by parts on Eq. (37) and defining pertinent shear correction matrixes by integrating in the z-direction results in,

$$\begin{aligned} \delta\Pi_{\tau_{xz}} =& \left[\mathcal{F}^T \boldsymbol{\eta}^{sbc^T} + \mathcal{F}_{,x}^T \boldsymbol{\eta}_x^{sbc^T} + \hat{T}_b \boldsymbol{\chi}^{sbc^T} \right] \Big|_{x_A}^{x_B} \delta\mathcal{F} + \\ & \int \left[\mathcal{F}^T \boldsymbol{\eta}^{s^T} + \mathcal{F}_{,x}^T \boldsymbol{\eta}_x^{s^T} + \mathcal{F}_{,xx}^T \boldsymbol{\eta}_{xx}^{s^T} + \hat{T}_b \boldsymbol{\chi}^{s^T} + \hat{T}_{b,x} \boldsymbol{\chi}_x^{s^T} \right] \delta\mathcal{F} \mathrm{d}x \end{aligned} \tag{38}$$

where all $\boldsymbol{\eta}_\alpha^s$ are $\mathcal{O}$x$\mathcal{O}$ matrixes of shear coefficients that automatically include pertinent shear correction factors. Matrixes $\boldsymbol{\chi}_\alpha^s$ are $\mathcal{O}$x1 column vectors of correction factors that enforce transverse shearing effects of the surface shear tractions. In each case the additional superscript bc refers to coefficients used in the boundary conditions. The size of these maxtrixes depends on the chosen order of the theory. For example a first-order shear theory has $\mathcal{O} = 2$ with in-plane stress resultant N and bending stress resultant M, i.e. $\mathcal{F} = \begin{bmatrix} N & M \end{bmatrix}^T$, while a third-order zigzag theory has has $\mathcal{O} = 6$ with in-plane stress resultants N, O, bending stress resultants M, P and zig-zag resultant $F_{\phi,x}, F_\phi$, i.e. $\mathcal{F} = \begin{bmatrix} N & M & O & P & F_{\phi,x} & F_\phi \end{bmatrix}^T$. The transposes of the different shear coefficient matrixes $\boldsymbol{\eta}_\alpha^{s^T}$ and $\boldsymbol{\chi}_\alpha^{s^T}$ are defined as follows

$$\boldsymbol{\eta}^{s^T} = \int_{-t/2}^{t/2} \left[-\left(\boldsymbol{c}^{(k)} \boldsymbol{s} \right)_{,xx}^T \frac{1}{G_{xz}^{(k)}} \boldsymbol{c}^{(k)} \boldsymbol{s} - \left(\boldsymbol{c}^{(k)} \boldsymbol{s} \right)_{,x}^T \left(\frac{1}{G_{xz}^{(k)}} \right)_{,x} \boldsymbol{c}^{(k)} \boldsymbol{s} \right] \mathrm{d}z \tag{39a}$$

$$\boldsymbol{\eta}_x^{s^T} = \int_{-t/2}^{t/2} \left[-\boldsymbol{s}^T \boldsymbol{c}^{(k)^T} \left(\frac{1}{G_{xz}^{(k)}} \right)_{,x} \boldsymbol{c}^{(k)} \boldsymbol{s} - 2 \left(\boldsymbol{c}^{(k)} \boldsymbol{s} \right)_{,x}^T \frac{1}{G_{xz}^{(k)}} \boldsymbol{c}^{(k)} \boldsymbol{s} \right] \mathrm{d}z \tag{39b}$$

$$\boldsymbol{\eta}_{xx}^{s^T} = \int_{-t/2}^{t/2} \left[-\boldsymbol{s}^T \boldsymbol{c}^{(k)^T} \frac{1}{G_{xz}^{(k)}} \boldsymbol{c}^{(k)} \boldsymbol{s} \right] \mathrm{d}z = -\boldsymbol{\eta}_x^{sbc^T} \tag{39c}$$

$$\boldsymbol{\chi}^{s^T} = \int_{-t/2}^{t/2} \left[-\left(\frac{1}{G_{xz}^{(k)}} \right)_{,x} \boldsymbol{c}^{(k)} \boldsymbol{s} \right] \mathrm{d}z \tag{39d}$$

$$\boldsymbol{\chi}_x^{s^T} = \int_{-t/2}^{t/2} \left[-\frac{1}{G_{xz}^{(k)}} \boldsymbol{c}^{(k)} \boldsymbol{s} \right] \mathrm{d}z = -\boldsymbol{\chi}^{sbc^T} \tag{39e}$$

$$\boldsymbol{\eta}^{sbc^T} = \int_{-t/2}^{t/2} \left[\left(\boldsymbol{c}^{(k)} \boldsymbol{s} \right)_{,x}^T \frac{1}{G_{xz}^{(k)}} \boldsymbol{c}^{(k)} \boldsymbol{s} \right] \mathrm{d}z. \tag{39f}$$

For the potential of transverse normal stress we expand the parentheses in Eq. (35c) and take the first variation to get

$$\begin{aligned}
\delta\Pi_{\sigma_z} = \int \Bigg[& \mathcal{F}^T \left(\boldsymbol{e}^{(k)}\boldsymbol{s}\right)^T_{,xx} R^{(k)}_{13}\bar{Q}^{(k)}\boldsymbol{f}^{(k)}\boldsymbol{s} + \mathcal{F}^T_{,x}\left(\boldsymbol{e}^{(k)}\boldsymbol{s}\right)^T_{,x} R^{(k)}_{13}\bar{Q}^{(k)}\boldsymbol{f}^{(k)}\boldsymbol{s} + \\
& \frac{1}{2}\mathcal{F}^T_{,xx}\left(\boldsymbol{e}^{(k)}\boldsymbol{s}\right)^T R^{(k)}_{13}\bar{Q}^{(k)}\boldsymbol{f}^{(k)}\boldsymbol{s} - \hat{T}_{b,x}\left(z-z_0\right) R^{(k)}_{33}\left(\boldsymbol{e}^{(k)}\boldsymbol{s}\right)_{,xx} + \hat{P}_b R^{(k)}_{33}\left(\boldsymbol{e}^{(k)}\boldsymbol{s}\right)_{,xx} - \\
& \frac{1}{2}\hat{T}_{b,x}\left(z-z_0\right) R^{(k)}_{13}\bar{Q}^{(k)}\boldsymbol{f}^{(k)}\boldsymbol{s} + \frac{1}{2}\hat{P}_b R^{(k)}_{13}\bar{Q}^{(k)}\boldsymbol{f}^{(k)}\boldsymbol{s} + \Bigg\{ \left(\boldsymbol{e}^{(k)}\boldsymbol{s}\right)_{,xx}\mathcal{F} + 2\left(\boldsymbol{e}^{(k)}\boldsymbol{s}\right)_{,x}\mathcal{F}_{,x} + \\
& \left(\boldsymbol{e}^{(k)}\boldsymbol{s}\right)\mathcal{F}_{,xx}\Bigg\}^T R^{(k)}_{33}\left(\boldsymbol{e}^{(k)}\boldsymbol{s}\right)_{,xx}\Bigg]\delta\mathcal{F}\mathrm{d}V + \int\Bigg[\mathcal{F}^T\boldsymbol{s}^T{\boldsymbol{f}^{(k)}}^T\bar{Q}^{(k)}R^{(k)}_{13}\left(\boldsymbol{e}^{(k)}\boldsymbol{s}\right)_{,x} - \\
& 2\hat{T}_{b,x}\left(z-z_0\right)R^{(k)}_{33}\left(\boldsymbol{e}^{(k)}\boldsymbol{s}\right)_{,x} + 2\hat{P}_b R^{(k)}_{33}\left(\boldsymbol{e}^{(k)}\boldsymbol{s}\right)_{,x} + 2\Bigg\{\left(\boldsymbol{e}^{(k)}\boldsymbol{s}\right)_{,xx}\mathcal{F} + \\
& 2\left(\boldsymbol{e}^{(k)}\boldsymbol{s}\right)_{,x}\mathcal{F}_{,x} + \left(\boldsymbol{e}^{(k)}\boldsymbol{s}\right)\mathcal{F}_{,xx}\Bigg\}^T R^{(k)}_{33}\left(\boldsymbol{e}^{(k)}\boldsymbol{s}\right)_{,x}\Bigg]\delta\mathcal{F}_{,x}\mathrm{d}V + \\
& \int\Bigg[\frac{1}{2}\mathcal{F}^T\boldsymbol{s}^T{\boldsymbol{f}^{(k)}}^T\bar{Q}^{(k)}R^{(k)}_{13}\left(\boldsymbol{e}^{(k)}\boldsymbol{s}\right) - \hat{T}_{b,x}\left(z-z_0\right)R^{(k)}_{33}\left(\boldsymbol{e}^{(k)}\boldsymbol{s}\right) + \hat{P}_b R^{(k)}_{33}\left(\boldsymbol{e}^{(k)}\boldsymbol{s}\right) + \\
& \Bigg\{\left(\boldsymbol{e}^{(k)}\boldsymbol{s}\right)_{,xx}\mathcal{F} + 2\left(\boldsymbol{e}^{(k)}\boldsymbol{s}\right)_{,x}\mathcal{F}_{,x} + \left(\boldsymbol{e}^{(k)}\boldsymbol{s}\right)\mathcal{F}_{,xx}\Bigg\}^T R^{(k)}_{33}\left(\boldsymbol{e}^{(k)}\boldsymbol{s}\right)\Bigg]\delta\mathcal{F}_{,xx}\mathrm{d}V. \qquad (40)
\end{aligned}$$

Next, the first and second derivatives are removed from the first variation of $\delta\mathcal{F}$ in Eq. (40) by using integration by parts, and pertinent transverse normal correction matrixes are defined by integrating in the z-direction to give,

$$\begin{aligned}
\delta\Pi_{\sigma_z} = & \Big[\mathcal{F}^T\boldsymbol{\eta}^{nbc^T} + \mathcal{F}^T_{,x}\boldsymbol{\eta}^{nbc^T}_x + \mathcal{F}^T_{,xx}\boldsymbol{\eta}^{nbc^T}_{xx} + \mathcal{F}^T_{,xxx}\boldsymbol{\eta}^{nbc^T}_{xxx} + \hat{T}_{b,x}\boldsymbol{\chi}^{nbc^T}_x + \hat{T}_{b,xx}\boldsymbol{\chi}^{nbc^T}_{xx} + \\
& \hat{P}_b\boldsymbol{\omega}^{nbc^T} + \hat{P}_{b,x}\boldsymbol{\omega}^{nbc^T}_x\Big]\Big|^{x_B}_{x_A}\delta\mathcal{F} + \Big[\mathcal{F}^T\boldsymbol{\rho}^{nbc^T} + \mathcal{F}^T_{,x}\boldsymbol{\rho}^{nbc^T}_x + \mathcal{F}^T_{,xx}\boldsymbol{\rho}^{nbc^T}_{xx} + \hat{T}_{b,x}\boldsymbol{\gamma}^{nbc^T}_x + \\
& \hat{P}_b\boldsymbol{\mu}^{nbc^T}\Big]\Big|^{x_B}_{x_A}\delta\mathcal{F}_{,x} + \int\Big[\mathcal{F}^T\boldsymbol{\eta}^{n^T} + \mathcal{F}^T_{,x}\boldsymbol{\eta}^{n^T}_x + \mathcal{F}^T_{,xx}\boldsymbol{\eta}^{n^T}_{xx} + \mathcal{F}^T_{,xxx}\boldsymbol{\eta}^{n^T}_{xxx} + \mathcal{F}^T_{,xxxx}\boldsymbol{\eta}^{n^T}_{xxxx} + \\
& \hat{T}_{b,x}\boldsymbol{\chi}^{n^T}_x + \hat{T}_{b,xx}\boldsymbol{\chi}^{n^T}_{xx} + \hat{T}_{b,xxx}\boldsymbol{\chi}^{n^T}_{xxx} + \hat{P}_b\boldsymbol{\omega}^{n^T} + \hat{P}_{b,x}\boldsymbol{\omega}^{n^T}_x + \hat{P}_{b,xx}\boldsymbol{\omega}^{n^T}_{xx}\Big]\delta\mathcal{F}\mathrm{d}x \qquad (41)
\end{aligned}$$

where all $\boldsymbol{\eta}^n_\alpha$ are $\mathcal{O}$x$\mathcal{O}$ matrixes of transverse normal coefficients that include pertinent correction factors. Matrixes $\boldsymbol{\chi}^n_\alpha$ and $\boldsymbol{\omega}^n_\alpha$ are $\mathcal{O}$x1 column vectors of correction factors that enforce transverse normal effects of the surface shear and normal tractions, respectively. Correction matrixes $\boldsymbol{\rho}^{nbc}_\alpha$, $\boldsymbol{\gamma}^{nbc}_x$ and $\boldsymbol{\mu}^{nbc}$ only appear in the boundary condition associated with $\delta\mathcal{F}_{,x}$. The full set of correction matrixes in Eq. (41) is defined as follows,

$$\begin{aligned}
\boldsymbol{\eta}^{n^T} = & \int_{-t/2}^{t/2}\Bigg[\left(\boldsymbol{e}^{(k)}\boldsymbol{s}\right)^T_{,xx}R^{(k)}_{13}\bar{Q}^{(k)}\boldsymbol{f}^{(k)}\boldsymbol{s} - \frac{1}{2}\boldsymbol{s}^T{\boldsymbol{f}^{(k)}}^T R^{(k)}_{13}\bar{Q}^{(k)}\left(\boldsymbol{e}^{(k)}\boldsymbol{s}\right)_{,xx} + \\
& \frac{1}{2}\left(\boldsymbol{f}^{(k)}\boldsymbol{s}\right)^T_{,xx}R^{(k)}_{13}\bar{Q}^{(k)}\boldsymbol{e}^{(k)}\boldsymbol{s} + \frac{1}{2}\boldsymbol{s}^T{\boldsymbol{f}^{(k)}}^T\left(R^{(k)}_{13}\bar{Q}^{(k)}\right)_{,xx}\boldsymbol{e}^{(k)}\boldsymbol{s} + \\
& \left(\boldsymbol{f}^{(k)}\boldsymbol{s}\right)^T_{,x}\left(R^{(k)}_{13}\bar{Q}^{(k)}\right)_{,x}\boldsymbol{e}^{(k)}\boldsymbol{s} + \left(\boldsymbol{e}^{(k)}\boldsymbol{s}\right)^T_{,xxxx}R^{(k)}_{33}\boldsymbol{e}^{(k)}\boldsymbol{s} + \left(\boldsymbol{e}^{(k)}\boldsymbol{s}\right)^T_{,xx}R^{(k)}_{33,xx}\boldsymbol{e}^{(k)}\boldsymbol{s} + \\
& 2\left(\boldsymbol{e}^{(k)}\boldsymbol{s}\right)^T_{,xxx}R^{(k)}_{33,x}\boldsymbol{e}^{(k)}\boldsymbol{s}\Bigg]\mathrm{d}z \qquad (42a)
\end{aligned}$$

$$\begin{aligned}
\boldsymbol{\eta}^{n^T}_x = & \int_{-t/2}^{t/2}\Bigg[\left(\boldsymbol{e}^{(k)}\boldsymbol{s}\right)^T_{,x}R^{(k)}_{13}\bar{Q}^{(k)}\boldsymbol{f}^{(k)}\boldsymbol{s} + \left(\boldsymbol{f}^{(k)}\boldsymbol{s}\right)^T_{,x}R^{(k)}_{13}\bar{Q}^{(k)}\boldsymbol{e}^{(k)}\boldsymbol{s} + \boldsymbol{s}^T{\boldsymbol{f}^{(k)}}^T\left(R^{(k)}_{13}\bar{Q}^{(k)}\right)_{,x}\boldsymbol{e}^{(k)}\boldsymbol{s} + \\
& 4\left(\boldsymbol{e}^{(k)}\boldsymbol{s}\right)^T_{,xxx}R^{(k)}_{33}\boldsymbol{e}^{(k)}\boldsymbol{s} + 2\left(\boldsymbol{e}^{(k)}\boldsymbol{s}\right)^T_{,x}R^{(k)}_{33,xx}\boldsymbol{e}^{(k)}\boldsymbol{s} + 6\left(\boldsymbol{e}^{(k)}\boldsymbol{s}\right)^T_{,xx}R^{(k)}_{33,x}\boldsymbol{e}^{(k)}\boldsymbol{s}\Bigg]\mathrm{d}z \qquad (42b)
\end{aligned}$$

$$\begin{aligned}
\boldsymbol{\eta}^{n^T}_{xx} = & \int_{-t/2}^{t/2}\Bigg[\frac{1}{2}\boldsymbol{s}^T{\boldsymbol{e}^{(k)}}^T R^{(k)}_{13}\bar{Q}^{(k)}\boldsymbol{f}^{(k)}\boldsymbol{s} + \frac{1}{2}\boldsymbol{s}^T{\boldsymbol{f}^{(k)}}^T R^{(k)}_{13}\bar{Q}^{(k)}\boldsymbol{e}^{(k)}\boldsymbol{s} + 6\left(\boldsymbol{e}^{(k)}\boldsymbol{s}\right)^T_{,xx}R^{(k)}_{33}\boldsymbol{e}^{(k)}\boldsymbol{s} +
\end{aligned}$$

$$6\left(\boldsymbol{e}^{(k)}\boldsymbol{s}\right)_{,x}^{T} R_{33,x}^{(k)}\boldsymbol{e}^{(k)}\boldsymbol{s} + \boldsymbol{s}^{T}\boldsymbol{e}^{(k)^{T}} R_{33,xx}^{(k)}\boldsymbol{e}^{(k)}\boldsymbol{s}\Big]\,\mathrm{d}z \tag{42c}$$

$$\boldsymbol{\eta}_{xxx}^{n^{T}} = \int_{-t/2}^{t/2}\left[4\left(\boldsymbol{e}^{(k)}\boldsymbol{s}\right)_{,x}^{T} R_{33}^{(k)}\boldsymbol{e}^{(k)}\boldsymbol{s} + 2\boldsymbol{s}^{T}\boldsymbol{e}^{(k)^{T}} R_{33,x}^{(k)}\boldsymbol{e}^{(k)}\boldsymbol{s}\right]\mathrm{d}z \tag{42d}$$

$$\boldsymbol{\eta}_{xxxx}^{n^{T}} = \int_{-t/2}^{t/2}\left[\boldsymbol{s}^{T}\boldsymbol{e}^{(k)^{T}} R_{33}^{(k)}\boldsymbol{e}^{(k)}\boldsymbol{s}\right]\mathrm{d}z = -\boldsymbol{\eta}_{xxx}^{nbc^{T}} = \boldsymbol{\rho}_{xx}^{nbc^{T}} \tag{42e}$$

$$\boldsymbol{\chi}_{x}^{n^{T}} = \int_{-t/2}^{t/2}(z-z_0)\left[-\frac{1}{2}R_{13}^{(k)}\bar{Q}^{(k)}\boldsymbol{f}^{(k)}\boldsymbol{s} - R_{33,xx}^{(k)}\boldsymbol{e}^{(k)}\boldsymbol{s}\right]\mathrm{d}z \tag{42f}$$

$$\boldsymbol{\chi}_{xx}^{n^{T}} = \int_{-t/2}^{t/2}(z-z_0)\left[-2R_{33,x}^{(k)}\boldsymbol{e}^{(k)}\boldsymbol{s}\right]\mathrm{d}z \tag{42g}$$

$$\boldsymbol{\chi}_{xxx}^{n^{T}} = \int_{-t/2}^{t/2}(z-z_0)\left[-R_{33}^{(k)}\boldsymbol{e}^{(k)}\boldsymbol{s}\right]\mathrm{d}z = -\boldsymbol{\chi}_{xx}^{nbc^{T}} = \boldsymbol{\gamma}_{x}^{nbc^{T}} \tag{42h}$$

$$\boldsymbol{\omega}^{n^{T}} = \int_{-t/2}^{t/2}\left[\frac{1}{2}R_{13}^{(k)}\bar{Q}^{(k)}\boldsymbol{f}^{(k)}\boldsymbol{s} + R_{33,xx}^{(k)}\boldsymbol{e}^{(k)}\boldsymbol{s}\right]\mathrm{d}z \tag{42i}$$

$$\boldsymbol{\omega}_{x}^{n^{T}} = \int_{-t/2}^{t/2}\left[2R_{33,x}^{(k)}\boldsymbol{e}^{(k)}\boldsymbol{s}\right]\mathrm{d}z, \quad \boldsymbol{\omega}_{xx}^{n^{T}} = \int_{-t/2}^{t/2}\left[R_{33}^{(k)}\boldsymbol{e}^{(k)}\boldsymbol{s}\right]\mathrm{d}z = -\boldsymbol{\omega}_{x}^{nbc^{T}} = \boldsymbol{\mu}^{nbc^{T}} \tag{42j}$$

$$\begin{aligned}\boldsymbol{\eta}^{nbc^{T}} = \int_{-t/2}^{t/2}\Bigg[&\frac{1}{2}\boldsymbol{s}^{T}\boldsymbol{f}^{(k)^{T}} R_{13}^{(k)}\bar{Q}^{(k)}\left(\boldsymbol{e}^{(k)}\boldsymbol{s}\right)_{,x} - \frac{1}{2}\left(\boldsymbol{s}^{T}\boldsymbol{f}^{(k)^{T}} R_{13}^{(k)}\bar{Q}^{(k)}\right)_{,x}\boldsymbol{e}^{(k)}\boldsymbol{s} + \\ &\left(\boldsymbol{e}^{(k)}\boldsymbol{s}\right)_{,xx}^{T} R_{33}^{(k)}\left(\boldsymbol{e}^{(k)}\boldsymbol{s}\right)_{,x} - \left\{\left(\boldsymbol{e}^{(k)}\boldsymbol{s}\right)_{,xx}^{T} R_{33}^{(k)}\right\}_{,x}\boldsymbol{e}^{(k)}\boldsymbol{s}\Bigg]\mathrm{d}z\end{aligned} \tag{42k}$$

$$\begin{aligned}\boldsymbol{\eta}_{x}^{nbc^{T}} = \int_{-t/2}^{t/2}\Bigg[&-\frac{1}{2}\boldsymbol{s}^{T}\boldsymbol{f}^{(k)^{T}} R_{13}^{(k)}\bar{Q}^{(k)}\boldsymbol{e}^{(k)}\boldsymbol{s} + 2\left(\boldsymbol{e}^{(k)}\boldsymbol{s}\right)_{,x}^{T} R_{33}^{(k)}\left(\boldsymbol{e}^{(k)}\boldsymbol{s}\right)_{,x} - \\ &3\left(\boldsymbol{e}^{(k)}\boldsymbol{s}\right)_{,xx}^{T} R_{33}^{(k)}\boldsymbol{e}^{(k)}\boldsymbol{s} - 2\left(\boldsymbol{e}^{(k)}\boldsymbol{s}\right)_{,x}^{T} R_{33,x}^{(k)}\boldsymbol{e}^{(k)}\boldsymbol{s}\Bigg]\mathrm{d}z\end{aligned} \tag{42l}$$

$$\boldsymbol{\eta}_{xx}^{nbc^{T}} = \int_{-t/2}^{t/2}\left[\boldsymbol{s}^{T}\boldsymbol{e}^{(k)^{T}} R_{33}^{(k)}\left(\boldsymbol{e}^{(k)}\boldsymbol{s}\right)_{,x} - 3\left(\boldsymbol{e}^{(k)}\boldsymbol{s}\right)_{,x}^{T} R_{33}^{(k)}\boldsymbol{e}^{(k)}\boldsymbol{s} - \boldsymbol{s}^{T}\boldsymbol{e}^{(k)^{T}} R_{33,x}^{(k)}\boldsymbol{e}^{(k)}\boldsymbol{s}\right]\mathrm{d}z \tag{42m}$$

$$\boldsymbol{\chi}_{x}^{nbc^{T}} = \int_{-t/2}^{t/2}(z-z_0)\left[-R_{33}^{(k)}\left(\boldsymbol{e}^{(k)}\boldsymbol{s}\right)_{,x} + R_{33,x}^{(k)}\boldsymbol{e}^{(k)}\boldsymbol{s}\right]\mathrm{d}z \tag{42n}$$

$$\boldsymbol{\omega}^{nbc^{T}} = \int_{-t/2}^{t/2}\left[R_{33}^{(k)}\left(\boldsymbol{e}^{(k)}\boldsymbol{s}\right)_{,x} - R_{33,x}^{(k)}\boldsymbol{e}^{(k)}\boldsymbol{s}\right]\mathrm{d}z \tag{42o}$$

$$\boldsymbol{\rho}^{nbc^{T}} = \int_{-t/2}^{t/2}\left[\frac{1}{2}\boldsymbol{s}^{T}\boldsymbol{f}^{(k)^{T}} R_{13}^{(k)}\bar{Q}^{(k)}\boldsymbol{e}^{(k)}\boldsymbol{s} + \left(\boldsymbol{e}^{(k)}\boldsymbol{s}\right)_{,xx}^{T} R_{33}^{(k)}\boldsymbol{e}^{(k)}\boldsymbol{s}\right]\mathrm{d}z \tag{42p}$$

$$\boldsymbol{\rho}_{x}^{nbc^{T}} = \int_{-t/2}^{t/2}\left[2\left(\boldsymbol{e}^{(k)}\boldsymbol{s}\right)_{,x}^{T} R_{33}^{(k)}\boldsymbol{e}^{(k)}\boldsymbol{s}\right]\mathrm{d}z. \tag{42q}$$

Finally, the potential of the Lagrange multipliers and the potential of contour loads are given by,

$$\begin{aligned}\delta\Pi_{\lambda} = &\int\left(N_{,x} + \hat{T}_t - \hat{T}_b\right)\delta\lambda_1\mathrm{d}x - \int\lambda_{1,x}\delta N\mathrm{d}x + \lambda_1\delta N|_{x_A}^{x_B} \\ &+ \int\left(M_{,xx} + z_N\hat{T}_{t,x} - z_0\hat{T}_{b,x} + \hat{P}_t - \hat{P}_b\right)\delta\lambda_2\mathrm{d}x \\ &+ \int\lambda_{2,xx}\delta M\mathrm{d}x + \lambda_2\delta M_{,x}|_{x_A}^{x_B} - \lambda_{2,x}\delta M|_{x_A}^{x_B}\end{aligned} \tag{43}$$

$$\delta\Pi_{\Gamma} = -\left[\delta\begin{bmatrix}\mathcal{F}_g^{T} & F_{\phi,x} & F_{\phi}\end{bmatrix}\cdot\begin{pmatrix}\hat{\mathcal{U}}_g\\0\\\psi\end{pmatrix} + \delta Q\hat{w}\right]\Bigg|_{x_A}^{x_B} = -\left[\delta\mathcal{F}^{T}\cdot\hat{\mathcal{U}}_{bc} + \delta M_{,x}\hat{w}\right]\Big|_{x_A}^{x_B}$$

$$= - \left[\delta \mathcal{F}^T \cdot \hat{\mathcal{U}}_{bc} + \delta \mathcal{F}^T_{,x} \hat{\mathcal{W}} \right] \Big|_{x_A}^{x_B} . \tag{44}$$

The integral expressions in equations (36), (38), (41), (43) and (44) combine to form the governing field equations (28), while the terms evaluated at $x = x_A$ and $x = x_B$ combine to form the governing boundary equations (29). These equations feature three column vectors $\mathbf{\Lambda}_{eq}, \mathbf{\Lambda}_{bc1}, \mathbf{\Lambda}_{bc2}$ that include the Lagrange multipliers λ_1, λ_2 and their derivatives. These are given by,

$$\mathbf{\Lambda}_{eq} = \begin{pmatrix} -\lambda_{1,x} \\ \lambda_{2,xx} \\ 0 \\ \vdots \end{pmatrix} , \; \mathbf{\Lambda}_{bc1} = \begin{pmatrix} \lambda_1 \\ -\lambda_{2,x} \\ 0 \\ \vdots \end{pmatrix} , \; \mathbf{\Lambda}_{bc2} = \begin{pmatrix} 0 \\ \lambda_2 \\ 0 \\ \vdots \end{pmatrix} . \tag{45}$$

The boundary displacement $\hat{w}$ in Eq. (44) is contained in the vector $\hat{\mathcal{W}} = \begin{bmatrix} 0 & \hat{w} & 0 & \dots \end{bmatrix}^T$.

References

[1] R M. Jones. *Mechanics of Composite Materials*. Taylor & Francis Ltd., London, UK, 2nd edition, 1998.

[2] S. Timoshenko. *Theory of Elasticity*. McGraw-Hill Book Company, Inc., New York, 1934.

[3] R D. Mindlin. Influence of rotary inertia and shear on flexural motion of isotropic elastic plates. *ASME Journal of Applied Mechanics*, 18:31–38, 1951.

[4] P C. Yang, C H. Norris, and Y. Stavsky. Elastic wave propagation in heterogeneous plates. *International Journal of Solids and Structures*, 2:665–684, 1966.

[5] J M. Whitney and N J. Pagano. Shear deformation in heterogeneous anisotropic plates. *Journal of Applied Mechanics*, 37:1031–1036, 1970.

[6] R M J. Groh and P M. Weaver. Static inconsistencies in certain axiomatic higher-order shear deformation theories for beams, plates and shells. *Composite Structures*, 120:231–245, 2015.

[7] E. Carrera. Theories and finite elements for multi- layered plates and shells: a unified compact formulation with numerical assessment and benchmarking. *Arch. Comput. Methods Eng.*, 10(3):5216–5296, 2003.

[8] L. Demasi. ∞^3 hierarchy plate theories for thick and thin composite plates: the generalized unified formulation. *Composite Structures*, 84:256–270, 2008.

[9] B F. Vlasov. On the equations of bending of plates. *Dokla. Ak. Nauk. Azerbeijanskoi-SSR*, 3:955–979, 1957.

[10] J N. Reddy. A refined nonlinear theory of plates with transverse shear deformation. *Int. J. Solids Structures*, 20(9):881–896, 1983.

[11] S A. Ambartsumyan. On theory of bending plates. *Isz. Otd. Tech. Nauk. AN SSSR*, 5:69–77, 1958.

[12] E. Reissner. On transverse bending of plates, including the effect of transverse shear deformation. *International Journal of Solids and Structures*, 11:569–573, 1975.

[13] J N. Reddy. A refined shear deformation theory for the analysis of laminated plates. Contractor Report 3955, National Aeronautics and Space Administration, 1986.

[14] M. Levy. Memoire sur la theorie des plaques elastique planes. *J. Math. Pures. Appl.*, 30:219–306, 1877.

[15] M. Stein. Nonlinear theory for plates and shells including the effect of transverse shearing. *AIAA Journal*, 24:1537–1544, 1986.

[16] M. Touratier. An efficient standard plate theory. *Int. J. Eng. Sci.*, 29:901–916, 1991.

[17] M. Karama, B. Abou Harb, S. Mistou, and S. Caperaa. Bending, buckling and free vibration of laminated composite with a transverse shear stress continuity model. *Composites Part B*, 29B:223–234, 1998.

[18] A J M. Ferreira, C M C. Roque, and R M N. Jorge. Analysis of composite plates by trigonometric shear deformation theory and multiquadrics. *Computers & Structures*, 83:2225–2237, 2005.

[19] K P. Soldatos. A transverse shear deformation theory for homogeneous monoclinic plates. *Acta. Mech.*, 94:195–220, 1992.

[20] A M A. Neves, A J M. Ferreira, E. Carrera, M. Cinefra, C M C. Roque, and R M N. Jorge. Free vibration analysis of functionally graded shells by a higher-order shear deformation theory and radial basis functions collocation, accounting for through-the-thickness deformations. *Eur. J. Mech, A - Solid*, 37:24–34, 2013.

[21] M. Karama, K S. Afaq, and S. Mistou. Mechanical behaviour of laminated composite beam by the new multi-layered laminated composite structures model with transverse shear stress continuity. *International Journal of Solids and Structures*, 40:1525–1546, 2003.

[22] J L. Mantari, A S. Oktem, and C. Guedes Soares. Static and dynamic analysis of laminated composite and sandwich plates and shells by using a new higher- order shear deformation theory. *Composites Structures*, 94:37–49, 2011.

[23] E. Reissner. On the theory of bending of elastic plates. *Journal of Mathematics and Physics*, 23:184–191, 1944.

[24] E. Reissner. The effect of transverse shear deformation on the bending of elastic plates. *Journal of Applied Mechanics*, 12(30):A69–A77, 1945.

[25] R C. Batra and S. Vidoli. Higher-order piezoelectric plate theory derived from a three-dimensional variational principle. *AIAA Journal*, 40(1):91–104, 2002.

[26] R C. Batra, S. Vidoli, and F. Vestroni. Plane wave solutions and modal analysis in higher order shear and normal deformable plate theories. *Journal of Sound and Vibration*, 257(1):63–88, 2002.

[27] E. Cosentino and P M. Weaver. An enhanced single-layer variational formulation for the effect of transverse shear on laminated orthotropic plates. *European Journal of Mechanics A/Solids*, 29:567–590, 2010.

[28] A. Tessler, M. Di Sciuva, and M. Gherlone. Refinement of Timoshenko beam theory for composite and sandwich beams using zigzag kinematics. Technical Publication 215086, National Aeronautics and Space Administration, 2007.

[29] A. Tessler, M. Di Sciuva, and M. Gherlone. Refined zigzag theory for laminated composite and sandwich plates. Technical Publication 215561, National Aeronautics and Space Administration, 2009.

[30] A. Tessler, M. Di Sciuva, and M. Gherlone. Refined zigzag theory for homogeneous, laminated composite, and sandwich plates: A homogeneous limit methodology for zigzag function selection. Technical Publication 216214, National Aeronautics and Space Administration, 2010.

[31] A. Tessler, M. Di Sciuva, and M. Gherlone. A consistent refinement of first-order shear deformation theory for laminated composite and sandwich plates using improved zigzag kinematics. *Journal of Mechanics of Materials and Structures*, 5(2):341–367, 2010.

[32] R M J. Groh and P M. Weaver. On displacement-based and mixed-variational equivalent single layer theories for modelling highly heterogeneous laminated beams. *International Journal of Solids and Structures*, 59:147–170, 2015.

[33] H. Murakami. Laminated composite plate theory with improved in-plane responses. *ASME Journal of Applied Mechanics*, 53:661–666, 1986.

[34] R M J. Groh, P M. Weaver, S. White, G. Raju, and Z. Wu. A 2D equivalent single-layer formulation for the effect of transverse shear on laminated plates with curvilinear fibres. *Composite Structures*, 100:464–478, 2013.

[35] G. Raju, Wu Z., Kim B C., and Weaver P M. Prebuckling and buckling analysis of variable angle tow plates with general boundary conditions. *Composite Structures*, 94(9):2961–2970, 2012.

[36] C. Shu. *Differential Quadrature and its Application in Engineering*. Springer Verlag, 2000.

[37] Z. Gurdal and R. Olmedo. In-plane response of laminates with spatially varying fiber orientations: variable stiffness concept. *AIAA J.*, 31(4):751–758, 1993.

[38] P.P. Camanho, C.G. Dávila, and M.F. de Moura. Numerical Simulation of Mixed-Mode Progressive Delamination in Composite Materials. *Journal of Composite Materials*, 37(16):1415–1435, 2003.